Investigation of Halogen Bonding Interactions Through Solid-State Nuclear Magnetic Resonance and Nuclear Quadrupole Resonance.

By

Vincent Morin

A Thesis Submitted in Partial Fulfilment of the Requirements for the Degree of

Masters in Chemistry

Department of Chemistry and Biomolecular Sciences

University of Ottawa

Abstract

Electrostatic interactions such as halogen bonding and pnictogen bonding interactions have gained a lot of interest in the field of crystal engineering and pharmaceutical science. In the first part of this thesis, we expand our knowledge on anion coordinated halogen bonded cocrystals by looking at a series of cocrystals made from 3-iodoethynyl pyridine and 3-iodoethynylbenzoic acid. We utilize the power of mechanochemistry to create the new cocrystals made with phosphonium salts and use multinuclear solid-state nuclear magnetic resonance spectroscopy and X-ray diffraction and characterize them. We found that mechanochemistry is a fast and powerful tool to explore and synthesize new halogen bonded cocrystals and ^{31}P solid-state NMR is a rapid way to identify the formation of a cocrystal. In the second part, we look at the versatility of the pnictogen atom, specifically antimony, as a pnictogen bond donor and a halogen bond acceptor. We evaluate these electrostatic interactions with nuclear quadrupolar resonance and found that nuclear quadrupole resonance is a strong spectroscopy tool to probe these types of electrostatic interactions.

Acknowledgments

I would like to offer my sincere thanks to Dr. David Bryce for all the help and opportunities that he has given me throughout these past years. These past years were challenging and fulfilling. I gained a lot of knowledge and experience working with him. Also thank you to the present and past members of the Bryce Nation: César Leroy, Vijith Kumar, Patrick Szell, Scott Southern, Yijue Xu, Estelle Caron-Poulin, Dan Ni Zheng, Christelle Hajjar, Tamali Nag and Shugha Gunaga for their help, guidance and friendship. Thanks to my favourite undergrads: Michael Triglav, Maressa Bradshaw, Hashim AlSayed, Carl Rodrigue, Safaa Khiri and Florian Philippe.

Thank you to the X-ray facillity and NMR facillity: Dr. Bulat Gabidullin, Dr. Jeffrey Ovens, Dr. Peter Pallister and Dr. Glenn A. Facey for their help and enriching discussions.

Also, Thank you to Patrick, Josh, Jon and Sarah in the Richeson lab and Will and David in the Beauchemin lab for all these BBQ and wing night.

Merci à mes parents pour leur aide et leur soutient.

Contents

List of Figures

List of Tables

Nomenclature

η	Asymmetry Parameter
γ	Gyromagnetic ratio
$\hbar$	Planck's Constant/(2π)
ω_0	Larmor Frequency
$\mathbf{E}$	Electric field
$\mathbf{E}_0$	Incident electric field
$\mathbf{K}$	Wave number
B_0	Magnetic field
H_Z	Hertz s^{-1}
K_B	Boltzmann
m_I	The Z component of the angular momentum
N_α	Lower level population
N_β	Upper level population
R_{PnB}	Normalized Bond length for Pnictogen Bonding Interaction
R_{XB}	Normalized Bond length for Halogen Bonding Interaction

T Temperature

3IEBA 3-iodoethynylbenzoic Acid

3IEP 3-iodoethynylpyridine

Å Angstrom

Cq Quadrupolar Coupling Constant

CSA Chemical Shift Anisotropy

E Energy

FID Free induction decay

MAS Magic Angle Spinning

NMR Nuclear Magnetic Resonance

NQR Nuclear Quadrupolar Resonance

ppm Parts per million

PXRD Powder X-ray Diffraction

Q Quadrupole Moment

QI Quadrupolar Interaction

SCXRD Single X-ray Diffraction

SSNMR Solid-State Nuclear Magnetic Resonance

Chapter 1

Introduction

Electrostatic interaction strength can vary according to the type of interaction such as Van der Waals forces, London dispersion forces and pi-stacking. However, the fundamental idea stays the same, and can be explained by Coulomb's law of electrostatics which states that positive and negative charges attract each other while same charges repel each other.[1] These types of interactions are present in nature. They appear in our DNA, which gives rise to the double helix configuration and keeps water in the liquid state at room temperature.[2]

1.1 Mechanochemistry

Mechanochemistry is a synthetic pathway in which reactants are physically put together to react and create new products. The reactants go under chemical change due to the mechanical force applied. Different types of forces can be used to generate new compounds such as ball milling, shearing, pulling and ultrasound.

Mechanochemistry has existed for centuries or even millennia in one form or another. It goes back to Theophrastus in 315 B.C, where in his book "On Stones",[3] he describes the reduction of cinnabar to mercury by grinding in a copper mortar with a copper pestle. Other important examples are the utilization of grinding and milling to process grains, minerals,

pharmaceuticals, black powder, etc. Those processes were accompanied by chemical changes. Later on in the 1800, Faraday described the reduction of silver chloride by grinding it with zinc, tin, iron, and copper in a mortar.[4] However, in the last decade, we have assisted to a resurgence of this process.[5–7] One important aspect of mechanochemistry and one explanation as to why it has reappeared is, without a doubt, its environmental aspect.[8] Chemical industries and pharmaceutical companies are looking for new methods which are greener, safer and more efficient to synthesise new compounds. For example, mechanochemistry that utilizes ball-milling is done in a closed system with no or a minimal amount of solvent, also without any heat. This technique can help reduce the emissions, waste and by products.[9]

The process used in this project was ball-milling. This technique consists of a stainless steel jar to which we add reactants with two ball bearings and then seal it shut. The jar is then fixed to a machine that vibrates at a set frequency for a given time. These jars can be made of different materials such as zirconium, tungsten carbide or Teflon. Ball-milling enables us to control the reactivity by monitoring the vibrating frequency and the mass of the ball bearing with respect to the sample.[10]

New mechanochemistry methods have been developed recently. More specifically, solvent assisted ball-milling[11, 12] where a small quantity of solvents is added to increase the reaction rate and to enhance the synthesis. The quantity of solvents that is added is measured in microliters (η in $\mu L/mg$). For dry ball-milling $\eta = 0$, for reactions in solution $\eta > 10\mu L/mg$, and for solvents assisted ball-milling, the η can range between $0 < \eta < 1\mu L/mg$.

Recent advancements in the ball-milling mention the ability to follow in real time the evolution of the synthesis with powder X-ray diffraction through the ball-mill jar.[13, 14]

Mechanochemistry could also be used for organic chemistry. For example, it could be

used for organocatalytic transformations.[15] Mechanochemistry offers a completely different chemical environment compared to the traditional chemical reactions. Therefore, with this technique, complicated reactions and reactions that are less accessible could be done more easily.

There have been studies on the effect of temperature on ball-milling.[16] The studies show that the reaction rate is highly dependent on the temperature. With the help of real time powder X-ray diffraction, the quantity of reactants diminishes by a factor of six when the temperature is raised by 45°C.

Thus, mechanochemistry is a field of study in full expansion that sparks more and more interest.

1.2 Cocrystal

A cocrystal is a crystal made of two different molecules that are bounded together by a non covalent interaction.[17] Cocrystallization is a technique that is used to couple two different molecules into a new crystal structure. Cocrystallization can be performed by mixing two initial products, dissolving them and then letting the solvent slowly evaporate in order to create the crystals. Another method that can be used is mechanochemistry. Mechanochemistry has shown to be a suitable pathway in the preparation of cocrystals and other compounds, such as metal organic frameworks (MOF).[18] In chapter 2 of this thesis, we look at a series of halogen bonded cocrystasl made from two halogen bond donors: 3-Iodoethynylpyridine and 3-iodoethynylbenzoic acid and a series of phosphonium salts. These cocrystals were synthesized by mechanochemistry following the procedure in chapter 2.

1.3 Halogen Bond

Halogen bonds are a type of electrostatic interaction between a halogen (i.e.Cl, Br and I), and a Lewis base. The angle between the halogen covalently bounded to an electron withdrawing group and the Lewis base is around 150 deg to 180 deg as in the figure1.1

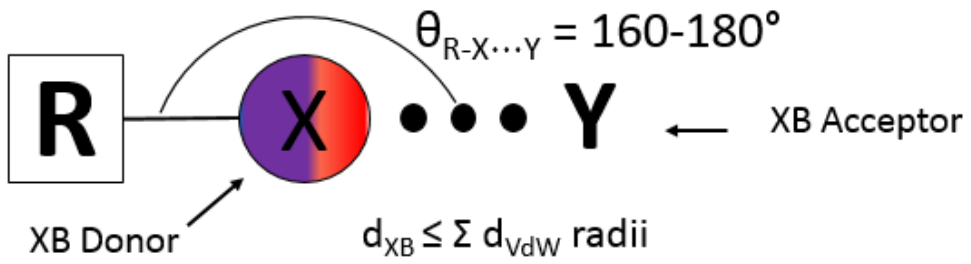

Figure 1.1: Visual representation of a halogen bond. X represents the halogen atom and R represents the electron withdrawing group. The red portion signifies the positive electrostatic region on the halogen.

. The length of the bond should be less than the sum of their Van der Waals radii. The equation 1.1[19] below allows to calculate the normalized bond length of the halogen bond:[19, 20]

$$R_{XB} = \frac{d_{X\cdots Y}}{\sum d_{\mathrm{vdW}}} \ , \tag{1.1}$$

where R_{XB} is the normalized bond length and the numerator is $d_{X\cdots Y}$ the distance of the halogen bond. The denominator is the summation of their Van der Waals radii. If the value of R_{XB} is smaller than 1, we can then confirm the presence of a halogen bond interaction. The intensity of this interaction increases as we go down the halogen group. For example, the intensity of the interaction will be higher for iodine than for chlorine. If we have a fluorine atom that is covalently bounded to an electron withdrawing group, the charge density around the fluorine atom will be negative. On the other hand, for bigger atoms such as chlorine, bromine and iodine that are covalently bounded to an electron withdrawing group, the charge density will have on the opposite side a positive region. This region is called σ-hole as shown

in figure 1.2.[21] Therefore, the bigger the σ-hole, the greater the interaction between the halogen atoms and the Lewis base.[22]

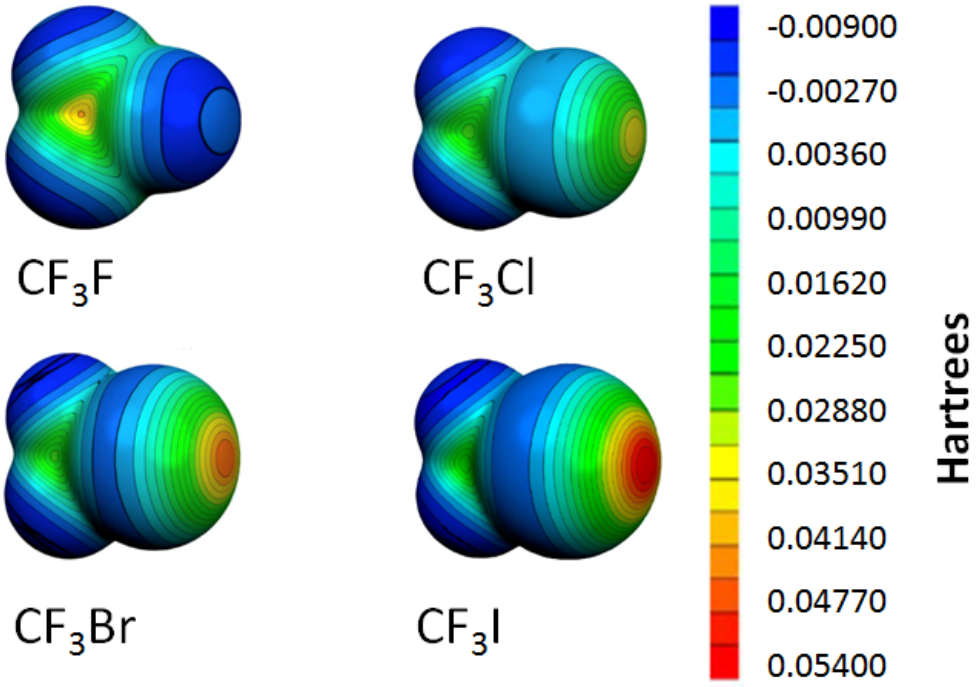

Figure 1.2: Visualisation of a σ-hole. Picture from Politzer et al.[21]

Since halogen bonding interaction is a growing field of research it would be important to look at some examples. The first halogen bonded interaction was between I_2 and NH_3, it was synthesized by J. J. Colin in the 1800. Since then countless examples have been reported in structural data based. One the commonly used halogen bond donor is 1,4-diiodotetrafluorobenzene. This Halogen bond donor have been shown to interacts with different acceptor from Cl- and Br- to 4,4'-dipyridine and triphenylphosphine selenide.[23] 1,4-diiodotetrafluorobenzene has other application other than crystal engineering, it's used as a catalys for the methyl group rotation in organic compounds.[24]

1.4 Nuclear Magnetic Resonance (NMR)

Nuclear magnetic resonance spectroscopy is based on the interaction of a magnetic field with the nuclei of an atom. The goal of this type of spectroscopy is to gain information on the electronic and chemical environment around the nucleus. This section will walk through the basics and how to apply them.

1.4.1 Spin

A nucleus has a intrinsic angular momentum called a spin I.[25] A spin has a quantum observable that has an amplitude of $(I(I+1))^{\frac{1}{2}}\hbar$. I can take values of 0 , $\frac{1}{2}$, 1 , $\frac{3}{2}$, $\cdots$. the Z component of the angular momentum is $m_I\hbar$, where m_I can take $2I+1$ with values going from $-I,\ -I+1,\ \cdots,\ I-1,\ I$. For example, a nucleus that has a spin of $I=\frac{1}{2}$, the possible values for for m_I are $m_I=\pm\frac{1}{2}$. For a nucleus that has an angular momentum of $I=1$, the possible values for the Z component of the angular momentum m_I are $-1, 0, 1$.

1.4.2 Zeeman Effect

In the absence of a magnetic field, the energy of the nucleus is independent from the orientation of the spin. When a magnetic field B_0 is applied in the Z axes, the energy of the nucleus depends on its orientation with respect to the applied magnetic field.[26] This leads to the splitting of the energy levels, and this phenomenon is called the Zeeman effect[25, 27] as shown in the figure 1.3.

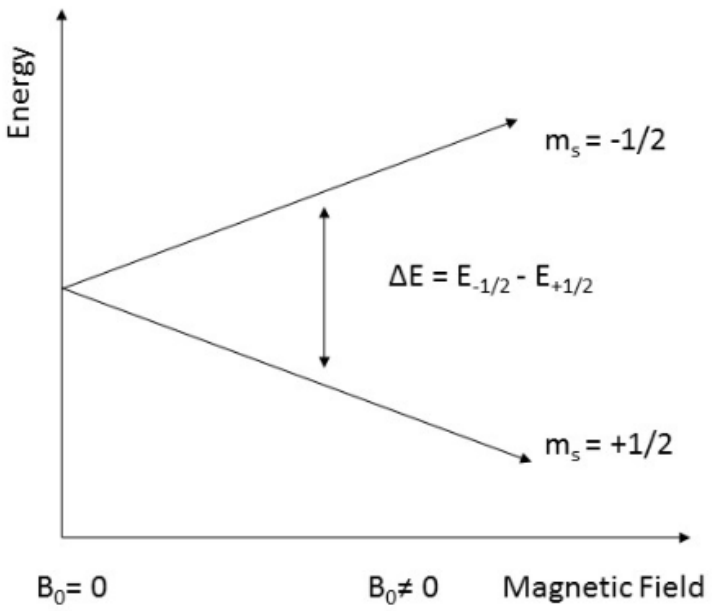

Figure 1.3: Visual representation of the Zeeman spliting

The interaction energy of a nuclei with a magnetic field B_0 that has a component m_I is given by

$$E = -\gamma m_I \hbar B_0 \,. \tag{1.2}$$

For a spin $\frac{1}{2}$ nucleus, there are two energy levels possible, $m_I = \pm\frac{1}{2}$. According to the equation 1.2, the lower energy level called α, has a component $m_I = +\frac{1}{2}$ (in the same orientation as the applied magnetic field) and an energy of

$$E_\alpha = -\frac{\gamma \hbar B_0}{2} \,,$$

while the higher energy level is called β, which has a component of $m_I = -\frac{1}{2}$ (aligned in the opposite direction as the applied magnetic field) and has an energy of,

$$E_\beta = \frac{\gamma \hbar B_0}{2} \,.$$

The difference between energy levels created by the Zeeman effect is

$$\Delta E = E_\beta - E_\alpha = \gamma \hbar B_0 \,. \tag{1.3}$$

Thus the difference between the energy levels are proportional to the strength of the applied magnetic field B_0.

A sample analyzed by NMR contains a lot molecules, we can thus talk about population. Because it is about quantified energy levels, the distribution function for the energy levels (N_α) and (N_β) is given by the Boltzmann distribution:[25]

$$\frac{N_\beta}{N_\alpha} = \exp\left(\frac{-\Delta E}{K_B T}\right) = \exp\left(\frac{-\gamma \hbar B_0}{K_B T}\right) , \tag{1.4}$$

where, $N = N_\alpha + N_\beta$, represents the total number of spins $\frac{1}{2}$ nuclei.

1.4.3 Larmor Frequency

The Larmor frequency is the frequency at which the nucleus precesses around the applied magnetic field.[25, 27] The Larmor frequency depends on the gyromagnetic ratio and the strength of the applied magnetic field as shown in this equation 1.5,

$$\omega_0 = \gamma B_0. \tag{1.5}$$

The Larmor frequency helps us calculate the radiofrequency at which we need to irradiate the sample to change the net magnetic moment.

1.4.4 Spin Precession and Data Acquisition

Spin precession is due to the interaction of the nuclear spin with a radio frequency pulse. The pulse frequency is calculated with the equation 1.5. For example, when a RF pulse is

applied to the sample 90 deg with respect to the magnetic field, the nuclear spin is projected in the XY plane and then starts to precess around the magnetic field to a lower energy state,[26, 27] as shown in the figure 1.4 below.

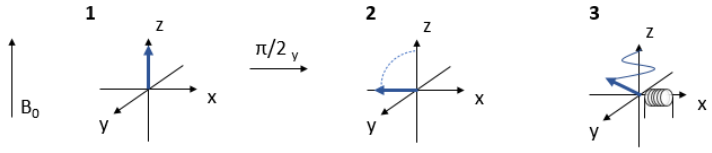

Figure 1.4: Visual representation of spin precession and data acquisition

This precession is caught by the NMR coil. The detection of precession of the magnetic moment of the sample results in a free induction decay or FID. The FID is the sum of all frequencies that are emitted by the nuclei of the sample. To be able to separate all the frequencies from the FID, you need to do a Fourier transform on the acquired signal to obtain an NMR spectrum.

1.4.5 Chemical Shift

Chemical shift is an important part of the NMR spectroscopy.[28, 29] Chemical shift is used to identify chemical compounds. The chemical shift results from a difference in resonance frequency which is caused by the shielding around the nucleus. The shielding is caused by the electron density around the nucleus. The resonance frequency of the nucleus can be calculated with this equation:[29]

$$\nu = \frac{\gamma}{2\pi} B_0(1-\sigma)\,, \tag{1.6}$$

where σ is the shielding constant around the nucleus. To convert the frequency in ppm, this formula is used:

$$\delta_{ppm} = \frac{\nu_{sample} - \nu_{ref}}{\nu_{ref}}\,. \tag{1.7}$$

TMS is used as a reference for ^{1}H and ^{13}C solution NMR.

Chemical shift gives us information on chemical environment around the nucleus which

helps us analyze electrostatic interactions.

1.4.6 Solid-State NMR

NMR is not just a solution state experiment, it can be applied to solids also.[28, 30, 31] Solid state NMR is more challenging because magnetic interactions are anisotropic, thus the interaction energy of the nuclear spin depends on its orientation with respect to the magnetic field. In other words, the frequency of the NMR signal depends on the orientation of the nucleus as shown in the following equation:

$$\nu = \frac{-\gamma B_0}{2\pi}[(1 - \sigma_{11}cos^2\theta_{11} + \sigma_{22}cos^2\theta_{22} + \sigma_{33}cos^2\theta_{33})]\,. \tag{1.8}$$

In this equation, σ_{ii} represents the principal component of the shielding tensor and θ_{ii} represents the angle between the principal components and the magnetic field B_0. In a solid state NMR experiment, all orientations of the crystal are represented which gives rise to a powder pattern as shown in figure 1.5 below.

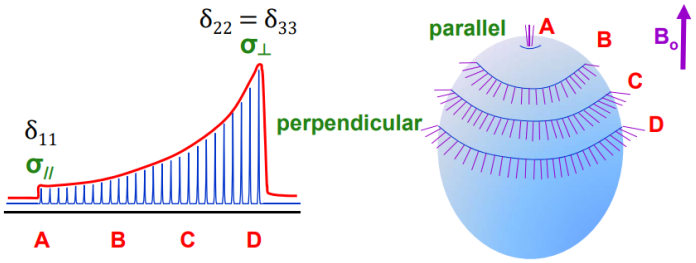

Figure 1.5: Chemical shift anisotropy (Picture given by Dr.Glenn A. Facey)

The chemical shielding tensor σ_{ii} can be expressed as a chemical shift anisotropy tensor (CSA) of three components $\delta_{11} \geq \delta_{22} \geq \delta_{33}$. The line shape caused by the CSA can be described by the isotropic chemical shift δ_{iso}, the span Ω and skew κ as shown in the following equation:

$$\delta_{iso} = \frac{\delta_{11} + \delta_{22} + \delta_{33}}{3} \tag{1.9}$$

$$\Omega = \delta_{11} - \delta_{33} \tag{1.10}$$

$$\kappa = \frac{3(\delta_{22} + \delta_{iso})}{\Omega}\,. \tag{1.11}$$

Solution state NMR does not exhibit these traits because of the rapid isotropic motion of the molecules in solution, which gives the isotropic value δ_{iso}. In solid state NMR, we can use a technique called MAS (Magic Angle Spinning) to mimic the solution state NMR spectra. MAS consists of spinning the sample at the magic angle which is 57.74°. This angle comes from the solution of the second Legendre polynomial as shown below:

$$P_2^0(\cos\theta) = \frac{1}{2}(3\cos^2\theta - 1)\,, \tag{1.12}$$

$$0 = 3(\cos^2\theta - 1)\,,$$

$$\theta = \cos^{-1}\sqrt{\frac{1}{3}}\,,$$

$$\theta = 54.74^\circ\,.$$

To be able to reduce the powder pattern to only one isotropic peak, you need to spin the sample at a frequency greater than the anisotropy of the interaction. If you spin the sample at a lower spinning speed, some spinning sidebands will emerge. These sidebands are sharp lines set at the spinning rate apart. The isotropic line is not always the central line or the most intense line, it is the only line that doesn't change when the spinning speed changes as shown in the figure 1.6 below.

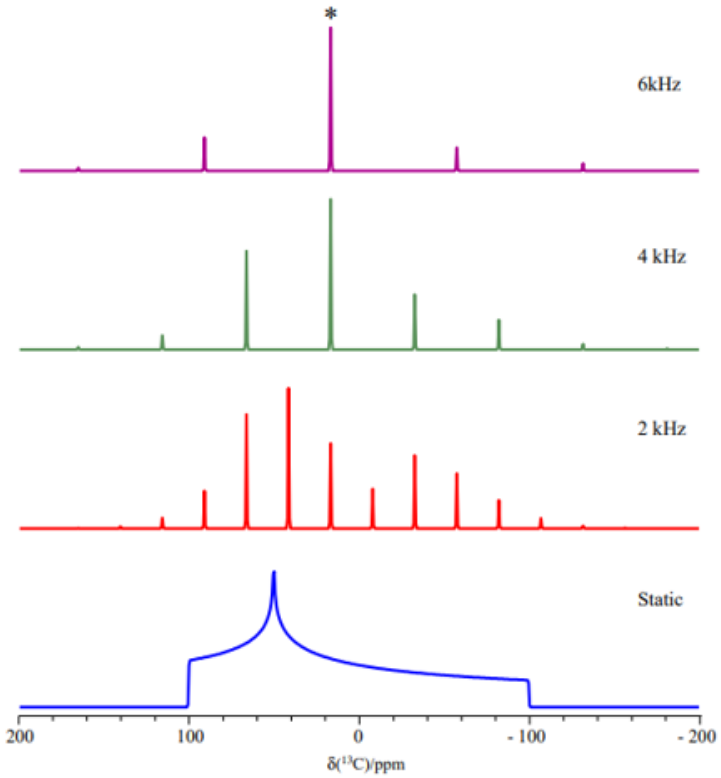

Figure 1.6: Simulated spectrum of ^{13}C at different spinning speed. The asterisk represents the isotropic peak

For nuclei such as ^{13}C and ^{31}P, you only expect to see one or two sidebands depending on the spinning speed. But other nuclei with a larger number of electrons have a greater chemical shift anisotropy, which means that even if you increase the spinning speed you will still observe many spinning sidebands SSNMR.

1.4.7 Cross-Polarisation

Cross-polarisation has become one of the most widely used techniques in solid-state NMR. Its main use is to observe low abundance nuclei such as ^{13}C. Usually diluted spins have a number of problems when trying to observe them. First, their low abundance means that the signal to noise ratio will be inevitably poor. Secondly, the low abundance nuclei tend to have very long relaxation time. This is largely due to the absence of the strong homonuclear interaction which helps stimulate relaxation. The longer relaxation time will ultimately effect

the time of the experiment. These problems can be solved by using the cross-polarisation pulse sequence as shown in the figure 1.7 below.

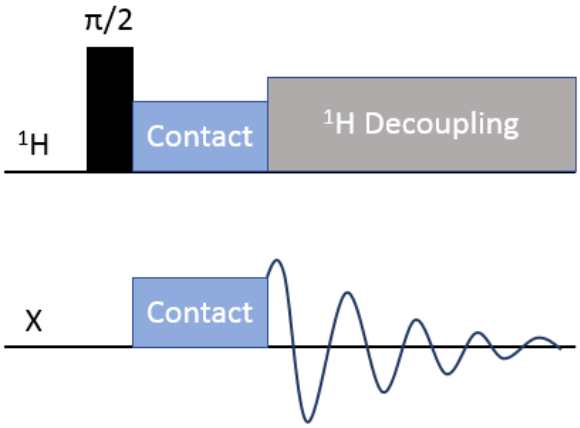

Figure 1.7: Graphical representation of cross polarisation pulse sequence

First, you apply a hard 90deg pulse on the protons to put them in the -y axis. At this point, the protons can precess around B_0. An on resonance contact pulse is applied on the -y axis, this creates a $B_1(H)$ field. This $B_1(H)$ field is called a spin lock field. It acts like the B_0 field, it helps to maintain the ^1H magnetization in the -y axis. The spin state on the protons can be described as a quantize where the spins of the protons are aligned with or against the applied $B_1(H)$ field. Now the X nuclei is also irradiated by a radio frequency which also creates a quantize spin state of the X nuclei. The spins are aligned with or against the applied $B_1(X)$ field. Thus, to be able to transfer the magnetization of the protons to the X nuclei, the amplitude of the contact pulse needs to be carefully matched to achieve the Hartmann-Hahn condition. In other words, as one proton spin relaxes an X spin gets magnetized following the conservation of energy rules. When the X nuclei are fully magnetized you then cut the matching pulse and decouple de protons and let X nuclei relax around the B_0 field.[32]

The experiments were done following the experimental procedure detailed in chapter 2 of the thesis.

1.4.8 Nuclear Quadrupolar Resonance

So far, we have only looked at spin 1/2 nuclei. Nevertheless, two thirds of all NMR active nuclei are quadrupolar, which means that they have a spin $I > 1/2$. Quadrupolar nuclei have an uneven distribution of charges which gives rise to a quadrupole moment (Q).[33] The value of the quadrupole moment can be positive or negative. A positive value indicates a prolate shape and a negative value indicates an oblate shape. In a nonsymmetrical environment, the Q will couple with the electric field gradient (EFG) leading to the quadrupolar coupling.[34] By measuring the quadrupolar coupling, it will give information on the EFG at the nucleus which can ultimately give information on the chemical environment.[35] The EFG can be described by a second rank tensor and it can be described by three orthogonal components such as V_{11}, V_{22} and V_{33}. These components are written by convention:

$$|V_{11}| \leq |V_{22}| \leq |V_{33}|. \tag{1.13}$$

And also these parameters respect Laplace equation which means that the sum equals zero, as shown in the equation below:

$$V_{11} + V_{22} + V_{33} = 0. \tag{1.14}$$

The quadrupolar coupling is described by two components which are the quadrupolar coupling constant denoted (Cq), it represents the intensity of the interaction. The other paramether is η which represents the asymmetry parameter and it is used to describe the shape.[36]

$$C_Q = \frac{eQV_{33}}{h} \tag{1.15}$$

$$\eta = \frac{V_{11} - V_{22}}{V_{33}} \tag{1.16}$$

In some cases, the quadrupolar interaction is so strong that even with the modern techniques in NMR spectroscopy, it makes it hard to perform analyses. In those special cases, nuclear quadrupolar resonance spectroscopy (NQR) becomes advantageous. NQR is performed in the absence of a magnetic field which means that the transition between the energy levels become degenerated. For example, a spin 5/2 nuclei will only have 2 transitions, as shown in the figure 1.8 below.

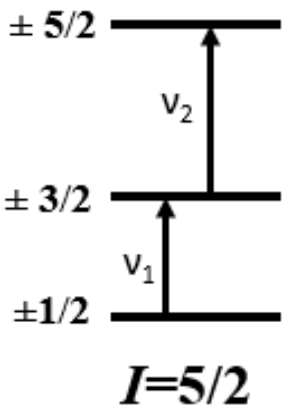

Figure 1.8: NQR transition for a spin 5/2 nucleus

These transitions have a relatively narrow linewidth. The resonance frequency of each transition is used to calculate the Cq and η. NQR spectroscopy coupled with computational calculation is a powerful tool to analyze and gain information on quadrupolar nuclei with strong quadrupolar coupling which otherwise would remain impossible to observe.[37]

The experiments were done following the experimental procedure detailed in chapter 3 of the thesis.

1.5 X-ray Diffraction

In this section we will take a look at the basic principle of X-ray diffraction and the interaction of X-ray with matter.

1.5.1 Powder X-ray Diffraction

The structure of materials can either be amorphous or crystalline. The perfect example of an amorphous structure is glass, and salt for a crystalline structure. X-ray diffraction is used to characterize a crystalline structure that was created during the cocrystallization step. X-ray diffraction is a method that is used in order to determine the structure of materials, and more specifically crystals. It is one of the most important tools used in the physics and material chemistry,[38].[39] This powerful tool enables us to characterize different aspects of a crystalline structure. Here are a few examples of its uses:

- 1. Determine the crystalline structure of crystals: the position of Bragg's peaks resulting from the powder X-ray diffraction indicates the reciprocal crystalline network to which the proper network can be determined.

- 2. Determine the degree of order or disorder in a crystal and its evolution in time: the width of the Bragg's peaks is inversely proportional to the correlation length of the order parameter (a variable that describes the amount of order in a system, it's typically used in the study of phase transitions). The size of the correlation length of the order parameter is inversely proportional to the average size of ordered material in the crystal. We can thus track the evolution in time of the order in a crystal by measuring the evolution of the width of the Bragg peak.

- 3. Identify the unknown materials by comparing their diffractogram to a known list of crystal structures.

- 4. Powder X-ray diffraction: identifying crystal formations, impurities, determining the size of the unit cells, and identifying polymorphs.

The basic principle of X-ray diffraction is based on the fact that an incident particle of light on a crystal will be deviated by the atoms forming the crystal, which will then reveal

the reciprocal crystal structure. In order to better understand the mechanism of X-ray diffraction, the following points will be discussed in greater detail:

- 1. The interaction of X-rays with matter.
- 2. The interaction of a beam of light (characterized by the electric field E) with a great number of atoms: we will show that this interaction is equivalent to performing a Fourier transform of the irradiated crystalline network.
- 3. Bragg's law which explains the phenomenon of interference due to the interaction of rays with crystalline network which leads to Bragg's peaks.

1.5.2 X-Ray Interaction with Matter

X-ray interaction with atoms is actually done with the electrons circling the atom. There are two classes of interactions, and three main types of X-ray interactions with electrons. These two classes are:

- 1. Elastic scattering: the incident ray and the scattered ray have the same wave length, only the propagation direction changes.
- 2. The inelastic scattering: the incident ray and the scattered ray do not have the same wave length.

The three main types of interactions are:

- 1. The Thompson scattering (elastic scattering): the electron oscillates like a dipole at the incident X-ray frequency. The scattered ray corresponds to the field emitted by the dipole.
- 2. The Compton scattering (inelastic scattering): quantum phenomenon where a photon collides with another electron and loses energy.

- 3. Photoionization (inelastic scattering): phenomenon where an electron can be dislodged from the atom following the absorption of a photon.

The phenomenon observed in X-ray diffraction is the Thompson scattering, an elastic scattering where the length of the incident rays, therefore the wave number, $k = \frac{2\pi}{\lambda}$, does not change. This phenomenon is illustrated in the figure 1.9.[39] The electric field of the X-ray is scattered by an angle 2θ by the electron oscillating like a dipole because of the incident electric field E_0.

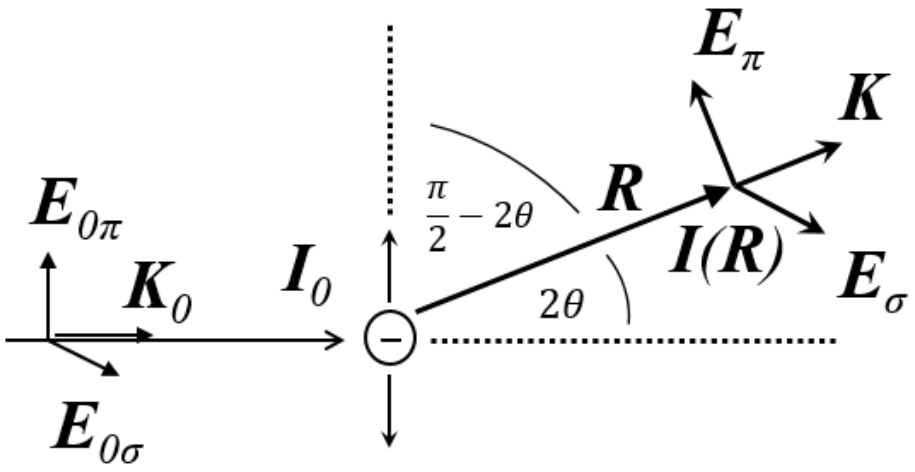

Figure 1.9: Thomson scattering: This figure represents the Thomson scattering model. A non-polarized X-ray beam of intensity I_0 (with electric field components $E_{0\sigma}$, $E_{0\pi}$ and with wave number K_0) interacts with an electron. Thomson scattering is an elastic process which implies that the magnitude of wave number K of the scattered rays is the same as K_0. E_σ, E_π are the intensity of the electric field components and $I(R)$ is the intensity of the scattered radiation at a distance R from the sample. 2θ is the angle between the incident direction of the X-rays and the direction where the scattering is observed

1.5.3 Bragg's Law

Bragg's law enables us to explain interference patterns that are generated by X-ray diffraction of crystals.

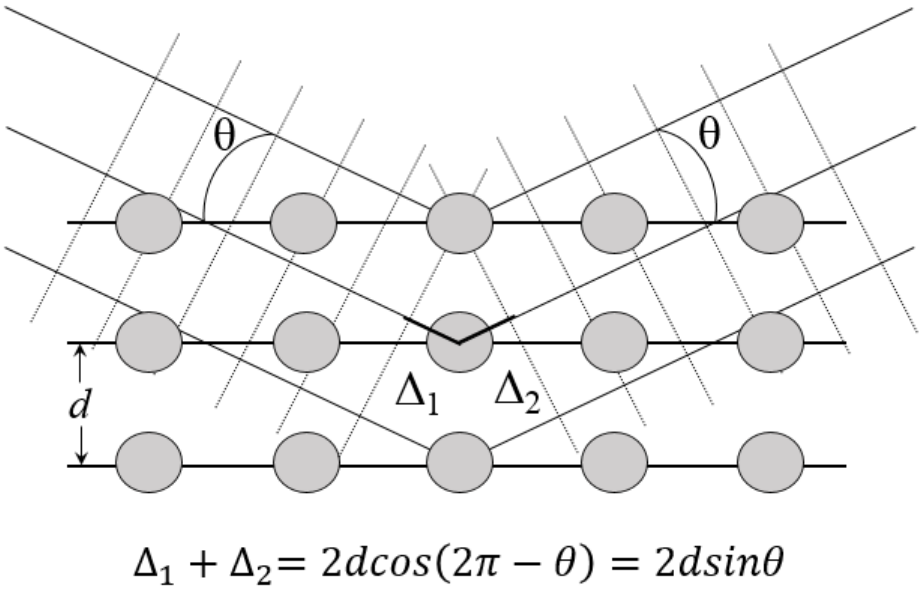

Figure 1.10: Bragg's law representation: θ is the angle of incidence of the X-ray on the crystal. $\Delta_1 + \Delta_2$ is the additional distance that the rays scattered by the second layer by the atoms in the sample travel compared to the first layer of the sample.

Bragg's law can be explained using simple rules of geometry (see figure 1.10[39]). If we consider layers of atoms at a distance d from one another and calculate the path difference between a ray hitting an atom of the first layer of the crystal and a ray hitting an atom from the layer directly underneath, we get:

$$\Delta_1 + \Delta_2 = 2d\sin(\theta), \tag{1.17}$$

where θ is the angle of the incident ray. For there to be constructive interference from the rays of the first layer and the second layer, the path difference has to be a number of wave length $n\lambda$:

$$n\lambda = 2d\sin(\theta), \tag{1.18}$$

This way, the wave peaks will hit the detector at the same time and will cause positive interference. There will be negative interference when the path difference is half a wave

length:

$$(n + \frac{1}{2})\lambda = 2d\sin(\theta), \tag{1.19}$$

For there to be an interference phenomenon, the wave length of the rays has to be of the order of the distance between the atoms of the crystal. The inter-atomic distance of the crystals and the molecules is typically of the order of 1,5 Angstrom to 4 Angstroms, which corresponds to an energy gap ranging from 3 keV to 8 keV.

The experiments were done following the experimental procedure detailed in chapter 2 of the thesis.

References

[1] R. P. Feynman, "Forces in Molecules," *Phys. Rev.*, vol. 56, pp. 340–343, Aug 1939.

[2] E. Arunan, G. R. Desiraju, R. A. Klein, J. Sadlej, S. Scheiner, I. Alkorta, D. C. Clary, R. H. Crabtree, J. J. Dannenberg, P. Hobza, H. G. Kjaergaard, A. C. Legon, B. Mennucci, and D. J. Nesbitt, "Definition of the hydrogen bond (IUPAC Recommendations 2011)," *Pure and Applied Chemistry*, vol. 83, no. 8, pp. 1637 – 1641, 08 Jul. 2011.

[3] A. Mottana, "The first modern translation of Theophrastus' "On Stones"(περι λιθων; De lapidibus): Ferrante Imperato (1599).," *Rend. Fis. Acc. Lincei*, vol. 21, pp. 1–25, 2010.

[4] L. Takacs, "The historical development of mechanochemistry," *Chem. Soc. Rev.*, vol. 42, pp. 7649–7659, 2013.

[5] L. Takacs, "The historical development of mechanochemistry," *Chem. Soc. Rev.*, vol. 42, pp. 7649–7659, 2013.

[6] J.-L. Do and T. Friščić, "Mechanochemistry: A Force of Synthesis," *ACS Central Science*, vol. 3, no. 1, pp. 13–19, 2017.

[7] J. G. Hernández, "Mechanochemistry," *Beilstein Journal of Organic Chemistry*, vol. 13, pp. 2372–2373, 2017.

[8] S. L. James and C. J. e. a. Adams, "Mechanochemistry: opportunities for new and cleaner synthesis," *Chemical Society Reviews*, vol. 41, pp. 413–447, 2012.

[9] C. Jimenez-Gonzalez, D. J. C. Constable, and C. S. Ponder, "Evaluating the Greenness of chemical processes and products in the pharmaceutical industry-a green metrics primer," *Chem. Soc. Rev.*, vol. 41, pp. 1485–1498, 2012.

[10] R. Schmidt, C. F. Burmeister, M. Baláž, A. Kwade, and A. Stolle, "Effect of Reaction Parameters on the Synthesis of 5-Arylidene Barbituric Acid Derivatives in Ball Mills," *Organic Process Research and Development*, vol. 19, no. 3, pp. 427–436, 2015.

[11] T. Friščić and W. Jones, "Recent Advances in Understanding the Mechanism of Cocrystal Formation via Grinding," *Crystal Growth and Design*, vol. 9, no. 3, pp. 1621–1637, 2009.

[12] D. R. Weyna and S. et al., "Synthesis and Structural Characterization of Cocrystals and Pharmaceutical Cocrystals: Mechanochemistry vs Slow Evaporation from Solution," *Crystal Growth and Design*, vol. 9, no. 2, pp. 1106–1123, 2009.

[13] T. Friščić, I. B. Halasz, and et al., "Real-time and in situ monitoring of mechanochemical milling reactions," *Nat. Chem.*, vol. 5, pp. 66–73, 2013.

[14] P. A. Julien, K. Užarević, A. D. Katsenis, S. A. J. Kimber, T. Wang, O. K. Farha, Y. Zhang, J. Casaban, L. S. Germann, M. Etter, R. E. Dinnebier, S. L. James, I. Halasz, and T. Friščić, "In Situ Monitoring and Mechanism of the Mechanochemical Formation of a Microporous MOF-74 Framework," *Journal of the American Chemical Society*, vol. 138, no. 9, pp. 2929–2932, 2016.

[15] J. G. Hernandez and E. Juaristi, "Recent efforts directed to the development of more sustainable asymmetric organocatalysis," *Chem. Commun.*, vol. 48, pp. 5396–5409, 2012.

[16] K. Užarević and Štrukil et al., "Exploring the Effect of Temperature on a Mechanochemical Reaction by in Situ Synchrotron Powder X-ray Diffraction," *Crystal Growth and Design*, vol. 16, no. 4, pp. 2342–2347, 2016.

[17] P. M. J. Szell, J. Dragon, S. Zablotny, S. R. Harrigan, B. Gabidullin, and D. L. Bryce, "Mechanochemistry and cocrystallization of 3-iodoethynylbenzoic acid with nitrogen-containing heterocycles: concurrent halogen and hydrogen bonding," *New J. Chem.*, vol. 42, pp. 10493–10501, 2018.

[18] L. Tröbs and F. Emmerling, "Mechanochemical synthesis and characterisation of cocrystals and metal organic compounds," *Faraday Discuss.*, vol. 170, pp. 109–119, 2014.

[19] P. M. J. Szell and D. L. Bryce, *Solid-State NMR Studies of Halogen Bonding.* Cham: Springer International Publishing, 2016.

[20] P. M. J. Szell, B. Gabidullin, and D. L. Bryce, "1,3,5-Tri(iodoethynyl)-2,4,6-trifluorobenzene: halogen-bonded frameworks and NMR spectroscopic analysis," *Acta Crystallographica Section B*, vol. 73, no. 2, pp. 153–162, 2017.

[21] T. Clark, M. Hennemann, J. S. Murray, and P. Politzer, "Halogen bonding: the σ-hole," *Journal of Molecular Modeling*, vol. 13, pp. 291–296, 2007.

[22] B. V. Pandiyan, P. Deepa, and P. Kolandaivel, "Studies on the σ-hole bonds (halogen, chalcogen, pnicogen and carbon bonds) based on the orientation of crystal structure," *Molecular Physics*, vol. 114, no. 24, pp. 3629–3642, 2016.

[23] G. Cavallo, P. Metrangolo, R. Milani, T. Pilati, A. Priimagi, G. Resnati, and G. Terraneo, "The Halogen Bond," *Chemical Reviews*, vol. 116, no. 4, pp. 2478–2601, 2016.

[24] P. M. J. Szell, S. Zablotny, and D. L. Bryce, "Halogen bonding as a supramolecular dynamics catalyst," *Nat Commun*, vol. 10, no. 916, 2019.

[25] J. d. P. Peter Atkins, *Chimie Physique.* De Boeck, 4 ed., 2013.

[26] M. H. Levitt, *Spin dynamics: basics of nuclear magnetic resonance.* Wiley, 2 ed., 2002.

[27] R. M. Silverstein, F. X. Webster, D. J. Kiemle, and D. L. Bryce, *Identification spectrométrique de composés organique.* De Boeck, 3 ed., 2016.

[28] J. Keeler, *Understanding NMR Spectroscopy.* Wiley, 2 ed., 01 2013.

[29] R. K. Harris and E. D. Becker, "NMR Nomenclature: Nuclear Spin Properties and Conventions for Chemical Shifts—IUPAC Recommendations," *Journal of Magnetic Resonance*, vol. 22, no. 4, pp. 458 – 483, 2002.

[30] M. J. Duer, *Introduction to Solid-State NMR Spectroscopy.* Wiley-Blackwell, 1 ed., 07 2005.

[31] D. L. Bryce and R. E. Wasylishen, *Solid-State NMR, Rotational Resonance* . Oxford: Elsevier, 1999.

[32] M. J. Duer, *Introduction to Solid-State NMR Spectroscopy.* Blackwell, 1 ed., 2004.

[33] P. Pyykkö, "Year-2017 nuclear quadrupole moments," *Molecular Physics*, vol. 116, no. 10, pp. 1328–1338, 2018.

[34] R. V. Pound, "Nuclear Electric Quadrupole Interactions in Crystals," *Phys. Rev.*, vol. 79, pp. 685–702, Aug 1950.

[35] F. A. Perras, I. Korobkov, and D. L. Bryce, "NMR crystallography of sodium diphosphates: combining dipolar, shielding, quadrupolar, diffraction, and computational information," *CrystEngComm*, vol. 15, pp. 8727–8738, 2013.

[36] P. P. Man, *Quadrupole Couplings in Nuclear Magnetic Resonance, General.* American Cancer Society, 2006.

[37] C. M. Widdifield, A. D. Bain, and D. L. Bryce, "Definitive solid-state $^{185/187}Re$ NMR spectral evidence for and analysis of the origin of high-order quadrupole-induced effects for I = 5/2," *Phys. Chem. Chem. Phys.*, vol. 13, pp. 12413–12420, 2011.

[38] C. Kittel, *Introduction to solide State Physics.* Wiley, 5 ed., 1976.

[39] M. Birkholz, "Thin film analysis by X-ray scattering," *Journal of Applied Crystallography - J APPL CRYST*, pp. 925–926, 12 2006.

Chapter 2

Mechanochemical Preparations of Anion Coordinated Architectures Based on 3-iodoethynylpyridine and 3-iodoethynylbenzoic Acid

Vincent M. Morin, Patrick M.J. Szell, Estelle Caron-Poulin, Bulat Gabidullin, and David L. Bryce* Chemistry Open, 2019, 8, 1328-1336

*Author to whom correspondence may be addressed

Department of Chemistry and Biomolecular Sciences

University of Ottawa

10 Marie Curie Private

Ottawa, Ontario K1N 6N5

Canada

Tel: +1-613-562-5800 ext.2018; fax: +1-613-562-5170

Email: dbryce@uottawa.ca

2.1 Abstract

The halogen bond has previously been explored as a versatile tool in crystal engineering and anion coordination chemistry, with mechanochemical synthetic techniques having been shown to provide convenient routes towards cocrystals. In an effort to expand our knowledge on the role of halogen bonding in anion coordination, here we explore a series of cocrystals formed between 3-iodoethynylpyridine (**1**) and 3-iodoethynylbenzoic acid (**2**) with halide salts. In total, we report 6 new crystal structures prepared by mechanochemical ball milling, with all structures exhibiting C≡C-I···X^- (X = Cl, Br) halogen bonds. Whereas cocrystals featuring a pyridine group (**1**) favored the formation of discrete entities, cocrystals featuring a benzoic acid group (**2**) yielded an alternation of halogen and hydrogen bonds. The compounds studied herein were further characterized by ^{13}C and ^{31}P solid-state nuclear magnetic resonance, with the chemical shifts offering a clear and convenient method of identifying the occurrence of halogen bonding, using the crude product obtained directly from the mechanochemical ball milling. Whereas the ^{31}P chemical shifts were quickly able to identify the occurrence of cocrystallization, ^{13}C solid-state NMR diagnostic of both the occurrence of halogen bonding and of hydrogen bonding.

Keywords: Halogen bonding, hydrogen bonding, solid-state NMR, crystal engineering, X-ray crystallography

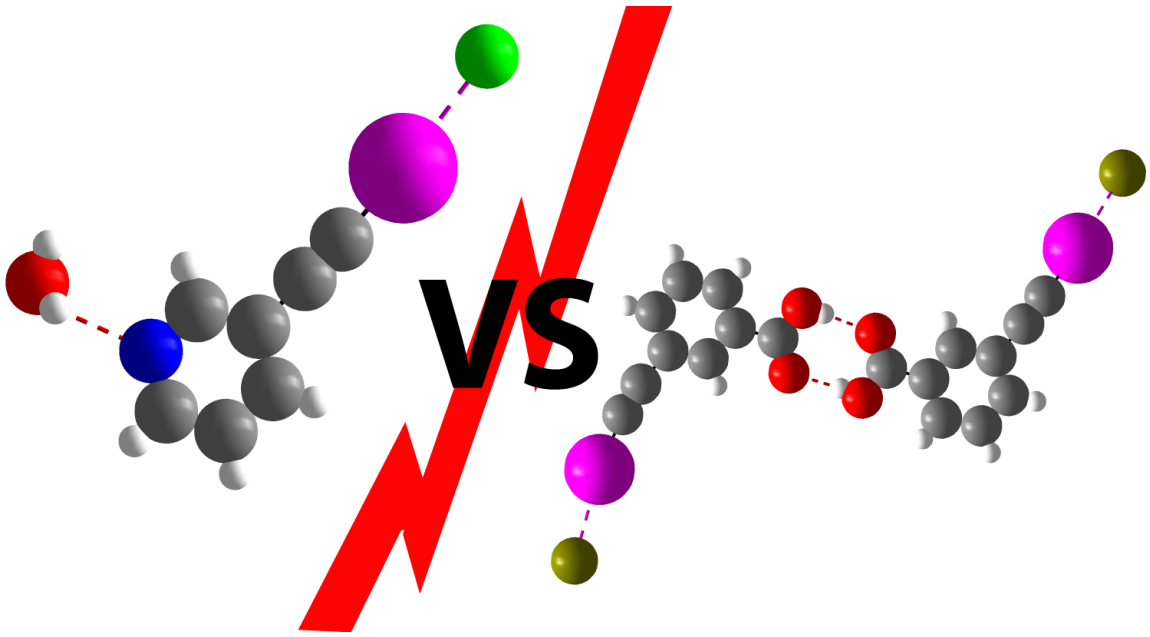

Figure 2.1: Cocrystal engineering using the 3-iodoethynyl moiety as a halogen bond donor is explored using mechanochemistry. X-ray diffraction and solid-state nuclear magnetic resonance spectroscopy highlight the roles of the halogen bonds and hydrogen bonds in determining the resulting structures.

Graphical Abstract

2.2 Introduction

The structural features of a crystalline framework can be modified in order to exhibit desirable properties, such as porosity[1, 2] and conductivity.[3, 4] The design of such modifications within the context of crystal engineering has gained popularity in recent years[5, 6] following a rational design approach rather than using brute force. Cocrystals, which typically combine two or more components interacting by means of non-covalent interactions,[7, 8] are a particular focus in the field crystal engineering. Rather than forming and breaking covalent bonds, structures can be tuned by individually modifying each component of the cocrystal, potentially reducing screening times. Several synthetic processes have been proposed to prepare cocrystals, such as mechanochemistry[9–11] and more recently, cosublimation,[12] yielding the

final product in as little as 10 minutes, all without the need of large solvent volumes.

Halogen bonding has been shown to be a powerful tool for crystal engineering.[13, 14] Halogen bonding, akin to hydrogen bonding,[15] is the attractive interaction between the region of increased electrostatic potential and reduced electron density[16] associated with a covalently bonded halogen, the σ-hole on the halogen bond donor,[17, 18] and a nucleophile, named the halogen bond acceptor.[19] The favourable characteristics of the halogen bond can be attributed to the strength of the interaction, varying with the size of the halogen (I > Br > Cl >> F),[20] and the presence of an electron withdrawing group.[21] An iodine-substituted sp-hybridized carbon, as found in the iodoacetylene functional group, is among the most activated halogen bond donor,[22] offering the potential to form strong halogen bonds. As a result, reports featuring halogen bonds to iodoacetylene groups have gained momentum due to potential uses in crystal engineering.[23–31]

Halogen bonding has become an important interaction for anion coordination (C-I···X; X = Cl^-, Br^-, I^-),[32]offering directional scaffolding for crystal engineering. Several crystal structures have been reported featuring anions coordinated by halogen bond donors, such as 1,4-diiodotetrafluorobenzene[33, 34] and 1,3,5-tri(iodoethynyl)-2,4,6-trifluorobenzene.[35, 36] This C-I···X^- motif has been shown to be of use in several classes of functional materials, such as halide recognition[37] and rotaxanes.[38] The preparation of cocrystals bearing the C-I···X^- halogen bonding motif by mechanochemistry has been previously exploited, offering the advantage of reduced preparation times.[39–42] In order to characterize the products, solid-state NMR (SSNMR) boasts the capability of offering structural information, such as identifying the occurrence of halogen bonding, and has been also shown to be useful in ensuring phase purity.[12]

We have previously investigated two iodoethynyl halogen bond donors: 3-iodoethynylpyridine (**1**)[43] and 3-iodoethynylbenzoic acid (**2**).[44] The previously reported crystal structure of **1** includes a self-complimentary zig-zag framework *via* C-I···N halogen bonds, while its halide salts favoured discrete charged dimers *via* C-I···X^- halogen bonding and N-H···X^- hydro-

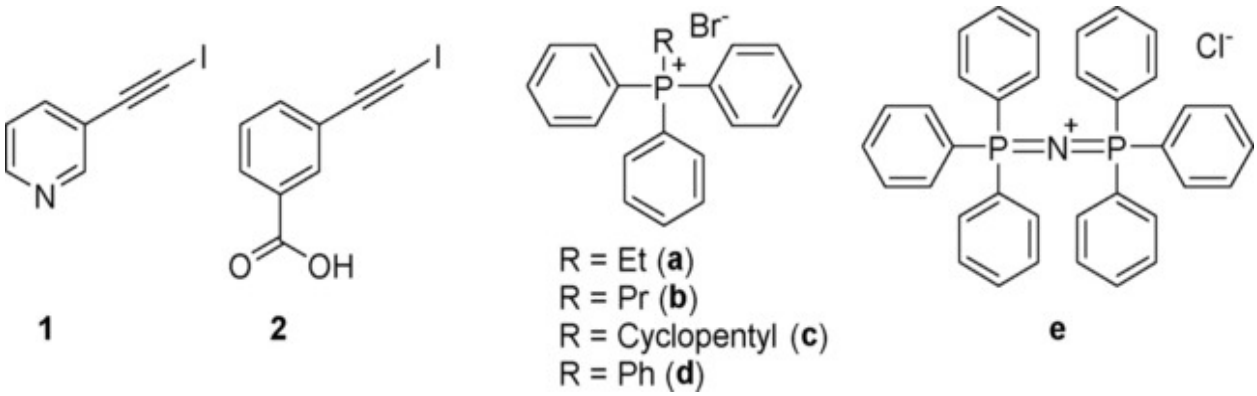

Figure 2.2: Molecular diagrams of the halogen bond donors (**1**, **2**) and the halide salts (**a** – **e**) used in this study. The R group denotes the substituent (ethyl, propyl, cyclopentyl, and phenyl).

gen bonding. In contrast, the structure of **2** displays simultaneous C-I···C halogen bonding with O-H···O hydrogen bonding. Moreover, upon the cocrystallization of **2** with a series of nitrogen-containing heterocycles, the resulting frameworks featured both C-I···N halogen bonds and O-H···O or O-H···N hydrogen bonds. Here, we turn our attention to investigate the potential of **1** and **2** in anion coordination using a series of halide salts as the halogen bond acceptors, with their molecular structures shown in Figure 2.2. We employ a mechanochemical approach to screening cocrystals, using ^{13}C and ^{31}P SSNMR to identify successful candidates, with a notable decrease in overall discovery time.

2.3 Experimental

3-ethynylbenzoic acid (95%), silver nitrate (99%), 3-ethynylpyridine (98%), ethyltriphenylphosphonium bromide (99%), tetraphenylphosphonium bromide (97%), propyltriphenylphosphonium bromide (98%) and potassium iodide (99%) were purchased from Sigma Aldrich. N-iodosuccinimide (97%), bis (triphenylphosphoranylidene) ammonium chloride (97%), cyclopentyltriphenylphosphonium bromide (98%) and *tert*-butyl hydroperoxide (70% aq. solution) were purchased from Alfa Aesar. Reagent grade acetone and acetonitrile were purchased from Fisher Scientific. All compounds were used without further purification. Both

1 and **2** were prepared from 3-ethynylpyridine and 3-ethynylbenzoic acid following literature procedures.[43, 44] The mechanochemical preparation of each of the cocrystals was performed using a Retsch MM400 ball mill. Both the halogen bond donor (**1**,**2**) and the appropriate halide salt (**a**–**e**) were added as powders successively to a 10 mL stainless steel milling jar in their proper stoichiometric ratio. All experimental masses and ratios can be found in Table S1 of the Supporting Information. Ball milling was performed with a milling frequency of 25 Hz for a period of 30 minutes at room temperature using two stainless steel grinding balls, in the presence of 10% M/M of acetonitrile. Crystals suitable for single crystal X-ray experiments were grown by dissolving the product obtained by ball milling in a minimum of acetonitrile, and allowing the solution to slowly evaporate. The phase purity of each compound was verified by powder X-ray diffraction on a Rigaku Ultima IV instrument with 2θ ranging from 5° to 55° at a rate of 1° per minute using CuKα radiation. All powder X-ray diffractograms can be found in the Supporting Information.

^{13}C Solid-State NMR. All ^{13}C cross-polarization magic-angle spinning (CP/MAS) solid-state NMR experiments were performed at 9.4 T ($\nu_{\mathrm{L}}(^{13}\mathrm{C}) = 100.6$ MHz) using a Bruker 4 mm HXY probe and a Bruker Avance III NMR spectrometer. $^{1}\mathrm{H} \rightarrow {}^{13}\mathrm{C}$ CP was used with a 3.6 µs proton $\pi/2$ pulse, a 2000 µs contact time, a recycle delay of 10 s, and a 69 kHz ^{1}H decoupling frequency. ^{13}C chemical shifts were referenced to glycine at 176.6 ppm (^{13}C=O) relative to tetramethylsilane (TMS). Variable spinning speeds were used to separate the spinning sidebands from the isotropic peaks. Further information, such as spinning speeds and the number of transients, can be found in the Supporting Information.

^{31}P Solid-State NMR. All ^{31}P cross-polarization magic-angle spinning (CP/MAS) solid-state NMR experiments were performed at 4.7 T ($\nu_{\mathrm{L}}(^{31}\mathrm{P}) = 80.961$ MHz) using a Bruker 7 mm HXY probe and a Bruker Avance III NMR spectrometer. $^{1}\mathrm{H} \rightarrow {}^{31}\mathrm{P}$ CP was used with a 3.75 µs proton pulse $\pi/2$ pulse, a 2000 µs contact time, and a 66.6 kHz ^{1}H decoupling frequency. ^{31}P chemical shifts were referenced to ammonium dihydrogen phosphate at 0.81 ppm. The MAS speed was set to 4 kHz.

Single Crystal X-Ray Diffraction.

The crystals were mounted on thin glass fibers using paraffin oil. Prior to data collection, crystals were cooled to 200 ± 2 K. The data was collected on a Bruker AXS single crystal diffractometer equipped with a sealed Mo tube source (wavelength 0.71073 Å) and an APEX II CCD detector. The raw data collection and processing were performed with the Bruker APEX II software package.[45] Semi-empirical absorption corrections based on equivalent reflections were applied.[46] Systematic absences in the diffraction dataset and unit cell parameters were consistent with triclinic $P\bar{1}$ (#2) for **1a**, monoclinic $P2_1/n$ (#14) for **2b**, **2e**, monoclinic $P2_1$/c (#14) for **1e**, orthorhombic *Pnma* (#62) for **2c**, and tetragonal $P\bar{4}2_1m$(#113) for **1b**. The structures were solved by direct methods and refined with full-matrix least-squares procedures based on F^2, using SHELXL[47] and WinGX.[48] All non-hydrogen atoms were refined anisotropically. The hydrogen atoms bonded to the oxygen atoms (**1e**, **2b**, **2e**) were located in the difference Fourier map and refined freely (**2b**, **2e**) or with certain restraints (**1e**) while the remaining hydrogen atoms were placed in idealized positions. Displacement ellipsoid plots were produced using ORTEP[49] (see the Supporting Information), and uncertainties were estimated using PLATON for Windows.[50] The structure of **1a** was refined without any additional restraints or constraints. In **1b** the 3-iodoethynylpyridine molecule lies on a mirror plane and its occupation is conventionally constrained at 0.5. The tetraphenylphosphonium cation lies on a 4-fold rotoinversion axis with the P atom on the inversion center; therefore, the P atom has a fixed 0.25 occupancy and the phenyl group is fully occupied. The Br anion lies on an intersection of two mirror planes; its occupancy is 0.25. In **1e**, both water molecules were refined using 1,2-distance (bond length) and 1,3-distance (bond angle) restraints (DFIX in SHELXL). The U_{iso} for H(1A), H(1B), H(2A), H(2B) atoms were constrained at $1.5\,U_{\mathrm{eq}}$ of the corresponding O atoms. In **2b** and **2e**, the H atoms of the carboxyl groups were refined freely without distance restraints nor ADP constraints. In **2c** the H(1A) atom of the carboxyl group was refined freely without distance restraints nor ADP constraints. The (cyclopentyl)triphenylphosphonium cation is located on a mirror plane. The

C(10)..C(15) phenyl ring is fully occupied and the P atom lies directly on the mirror plane and has a half occupancy. One of the three phenyl groups (two positions: C(16)..C(19) and C(20')..C(23')) and the cyclopentyl group (two positions: C(20)..C(22) and C(16')..C(18')) are disordered over two mutually overlapping positions with 0.568(9):0.432(9) occupancies. These disordered fragments were refined using a number of restraints due to the complexity of the case: bond distance restraints (SADI and DFIX in SHELXL), a planarity restraint (FLAT in SHELXL) applied to the P(1),C(16)..C(19) and P(1),C(20')..C(23') fragments, an 'equal ADP' (EADP in SHELXL) constraint applied to the C(16),C(16') and C(20),C(20') atom pairs due to their spatial proximity and overlap, enhanced rigid-bond restraints (RIGU in SHELXL) applied to the ADPs of the P(1),C(16)..C(19), and P(1),C(16')..C(18'), and P(1),C(20)..C(22), and P(1),C(20')..C(23') atom groups.

2.4 Results and Discussion

X-ray crystallography

Mechanochemical ball milling yielded powdered products in all cases. Following their identification by SSNMR (*vide infra*), a small portion of each product was subsequently dissolved and recrystallized by solvent evaporation in order to obtain crystals suitable for single crystal X-ray diffraction. A total of six X-ray crystal structures are reported here, with each structure exhibiting an iodine halogen bond to the anion of the halide salt (see Figure 2.3). Three structures feature **1** as the halogen bond donor, while the other three structures feature **2** as the halogen bond donor. The size of the cation in the salts varies, featuring short alkyl chains (**a**, **b**), rings (**c**, **d**), and finally a large cation (**e**). The purpose of these modifications was to relate the structural changes of the cation to the halogen bonding motif.

Structure **1a** reveals a single C-I···Br^- halogen bond between **1** and the bromide anion of **a** ($d_{I\cdots Br}$ = 3.1344(9) Å, $\theta_{C\text{-}I\cdots Br}$ = 171.12(10)°), forming a discrete halogen bonded entity

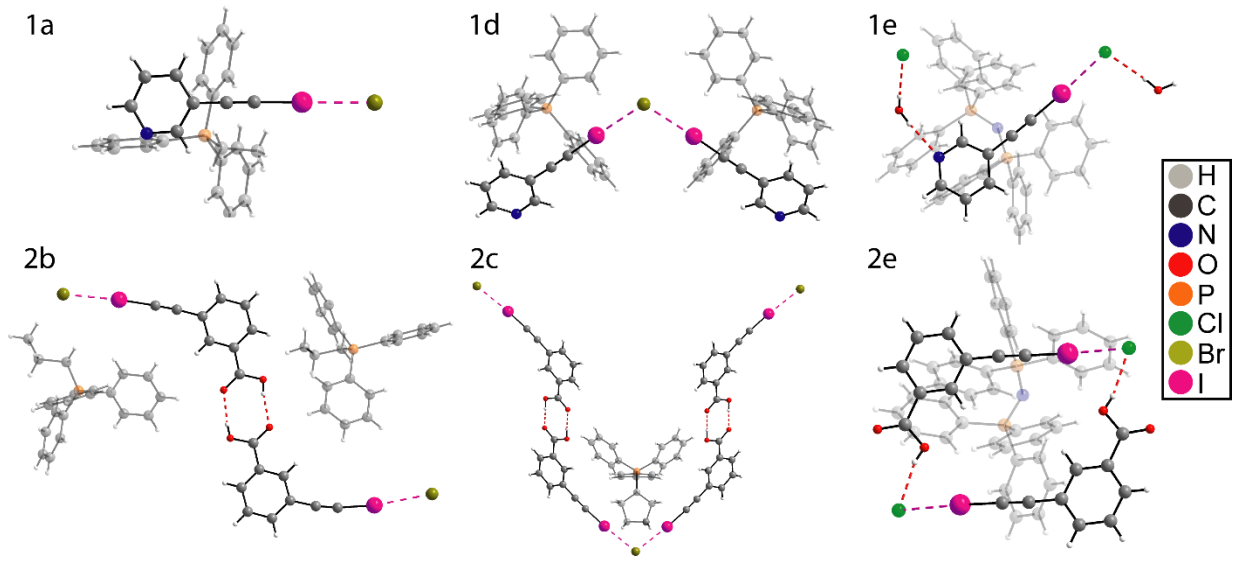

Figure 2.3: Depiction of the halogen and hydrogen bonding motifs in the crystal structures studied herein. The counter-ion is rendered transparent for clarity, highlighting the halogen/hydrogen bonding motifs. See text for further discussion.

rather than a continuous framework. In addition to the halogen bond, the bromide anion is engaged in several short H···Br contacts involving both the phosphonium cation of **a** and the proton in the *para* position relative to the nitrogen of the pyridine ring of **1**, encapsulating the anion. Further, the nitrogen atom on the pyridine ring of **1** is participating in two C-H···N hydrogen bonds ($d_{\text{H···N}}$ = 2.714 Å, $\theta_{\text{C-H···N}}$ = 167.18°; $d_{\text{H···N}}$ = 2.737 Å, $\theta_{\text{C-H···N}}$ = 135.95°), linking **1** to the phosphonium cation of **a**.

Cocrystal **1d** features a **1**···Br^-···**1** discrete halogen bonded dimer involving one crystallographically unique molecule of **1** ($d_{\text{I···Br}}$ = 3.2924(10) Å, $\theta_{\text{C-I···Br}}$ = 177.9(3)°), with an angle of $\theta_{\text{I···Br···I}}$ = 99.2° between the two halogen bonded fragments. In contrast to structure **1a**, the bromide anion displays no other close contacts and the nitrogen atom on the pyridine ring of **1** does not participate in hydrogen bonding. However, the proton in the *para* position relative to the nitrogen of **1** is participating in a H···C contact to the cation of **d** ($d_{\text{H···C}}$ = 2.855 Å), reflecting the same contact as observed in structure **1a**. The overall crystal packing, shown in Figure 2.4, reveals a cation of **d** surrounded by the halogen bonded dimer in a

unique square pattern exhibiting tetragonal symmetry. These patterns are stacked amongst each other, forming the crystal.

The crystal structure of **1e** features a large unit cell volume of 8263(12) Å^3, containing two molecules of PPNCl, two molecules of **1**, two water molecules, and two acetonitrile molecules. As a result, there are two crystallographically independent chloride anions, with each anion participating in a halogen bond with **1** and a hydrogen bond involving a water molecule. Following the labelling scheme of the crystal structure, there are five contacts to Cl(1): a halogen bond ($d_{\text{I}\cdots\text{Cl}}$ = 3.060(3) Å, $\theta_{\text{C-I}\cdots\text{Br}}$ = 174.61(15)°) with **1**, a hydrogen bond with water ($d_{\text{Cl}\cdots\text{H}}$ = 2.313 Å), two short contacts to the proton of the cation ($d_{\text{Cl}\cdots\text{H}}$ = 2.935 Å; $d_{\text{Cl}\cdots\text{H}}$ = 2.948 Å), and a short contact to the proton of acetonitrile ($d_{\text{Cl}\cdots\text{H}}$ = 2.653 Å). In contrast, Cl(2) participates in three contacts: a halogen bond ($d_{\text{I}\cdots\text{Cl}}$ = 3.102(3) Å, $\theta_{\text{C-I}\cdots\text{Br}}$ = 174.43(15)°) to **1**, a hydrogen bond to water ($d_{\text{Cl}\cdots\text{H}}$ = 2.294 Å), and a short contact to the proton of the cation ($d_{\text{Cl}\cdots\text{H}}$ = 2.766 Å). In addition to the I···Cl halogen bonds, both molecules of **1** participate in a N···H hydrogen bond involving the nitrogen atom on the pyridine ring ($d_{\text{N}\cdots\text{H}}$ = 2.281 Å; $d_{\text{N}\cdots\text{H}}$ = 2.182 Å). Overall, the alternation of I···Cl halogen bonds and N···H hydrogen bonds with **1** creates a unique framework, with a depiction shown in Figure 2.4. While the acetonitrile molecules form short N···H contacts between the cation and nitrogen of acetonitrile in addition to a Cl···H contact to the chloride anion, they do not appear to have a significant contribution to the overall framework. The crystal packs in alternating layers of the cation and halogen bonded fragments, building the overall crystal structure of **1e**.

2b includes two molecules of **2** and one molecule of **b** in the asymmetric unit. In addition to a I···Br halogen bond ($d_{\text{I}\cdots\text{Br}}$ = 3.1974(8) Å, $\theta_{\text{C-I}\cdots\text{Br}}$ = 170.71(12)°), **2** dimerizes *via* bridging O-H···O hydrogen bonding of the carboxylic acid groups, forming a Br···**2**···**2**···Br motif. The coordination sphere surrounding the Br^- anion includes two halogen bonds in a nearly linear configuration ($\theta_{\text{I}\cdots\text{Br}\cdots\text{I}}$ = 170.5°), in addition to three H···Br contacts involving the cation **b**. Both molecules of **2** in the hydrogen bonded dimer remain in the same

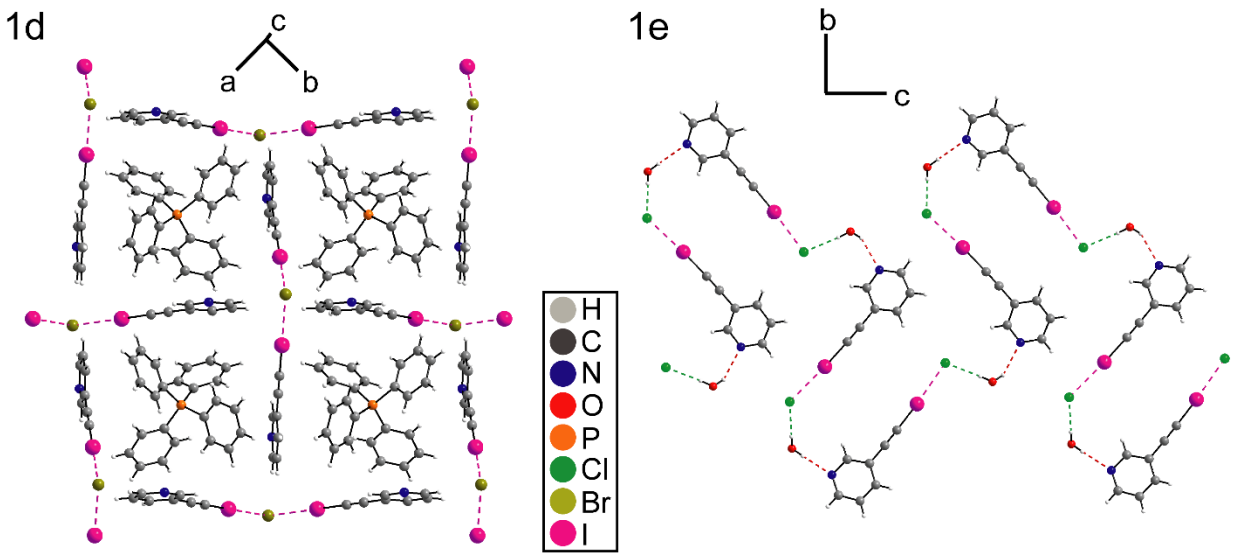

Figure 2.4: Depiction of the crystal packing of structure **1d** (left), and the halogen/hydrogen bonded fragment observed in structure **1e** (right). The dashed magenta lines denote the halogen bonds, the dashed red lines denote the H···N hydrogen bonds, and the dashed green lines denote H···Cl contacts. The cation in **1e** is not shown for clarity.

molecular plane. However, the molecular plane of the hydrogen-bonded dimers alternate at right angles between the halogen bonding linkers, forming a 3D zig-zag motif.

The crystal structure of compound **2c** exhibits a 1:1 molar ratio, in contrast to the 2:1 ratio observed in structure **2b**. Despite this difference in the stoichiometry, the molecules of **2** participate in a I···Br halogen bond ($d_{\text{I···Br}}$ = 3.1662(5) Å, $\theta_{\text{C-I···Br}}$ = 175.12(10)°) in addition to hydrogen bonding. In this case, however, the angle between both halogen bonds is $\theta_{\text{I···Br···I}}$ = 102.88°, with the overall motif consisting of a zig-zag pattern, shown in Figure 2.3. This pattern generates space between the halogen/hydrogen bonded fragments, which is occupied by the cation. In addition to the two C-I···Br$^-$ halogen bonds, the bromide anion is participating in five H···Br$^-$ contacts involving the cation. Further, the cation displays disorder between the cyclopentyl group and a phenyl group.

Cocrystal **2e** features one molecule of **2**, one molecule of **e**, and one molecule of acetonitrile in the asymmetric unit. Each molecule of **2** participates in a I···Cl halogen bond ($d_{\text{I···Br}}$ = 3.1187(13) Å, $\theta_{\text{C-I···Br}}$ = 173.37(13)°), in addition to a H···Cl hydrogen bond ($d_{\text{H···Cl}}$ = 2.239 Å) rather than forming dimers *via* O-H···O hydrogen bonding as observed in structures **2b**

Table 2.1: Halogen bond geometry of the cocrystals investigated herein

compound	XB moiety	XB length $(d_{I\cdots Y})$/Å	R_{XB} [a]	XB angle $\theta_{C-I\cdots Y}$ (°)
1a	$C-I\cdots Br^-$	3.1344(9)	0.82	171.12(10)
1d	$C-I\cdots Br^-$	3.2924(10)	0.86	177.9(3)
1e	$C-I\cdots Cl^-$	3.060(3)	0.82	174.61(15)
1e	$C-I\cdots Cl^-$	3.102(3)	0.83	174.43(15)
2b	$C-I\cdots Br^-$	3.1974(8)	0.83	170.71(12)
2c	$C-I\cdots Br^-$	3.1662(5)	0.83	175.12(10)
2e	$C-I\cdots Cl^-$	3.1187(13)	0.84	173.37(13)

[a]The normalized distance parameter was calculated using $R_{XB} = \frac{d_{I\bullet\bullet\bullet Y}}{\sum d_{vdW}}$ where Σd_{vdW} denotes the sum of the van der Waals radii.

and **2c**. As a result, a unique dimer is formed *via* both halogen and hydrogen bonds. In addition to a hydrogen bond and halogen bond, the chloride anion participates in a contact involving the proton of a nearby acetonitrile molecule. Much like structure **1e**, structure **2e** packs in alternating layers of the cation and halogen bonded fragments.

The halogen bond lengths observed in these structures, summarized in Table 2.1, are on the same order as previously reported structures featuring the iodoethynyl group coordinating halogen anions. For instance, the halogen bond lengths reported for the donor 1,3,5-tri(iodoethynyl)-2,4,6-trifluorobenzene coordinating a bromide anion are on the order of 3.1893(7) Å to 3.335(2) Å.[36] In contrast with our previous study on cocrystals featuring **2** with a series of nitrogen-containing heterocycles, the C-I···N halogen bond length varied between 2.741(6) Å to 3.021(3) Å,[44] notably shorter than the C-I···Br$^-$ distances observed herein. Further X-ray crystallographic details are given in Table 2.2,2.3 and in the Supporting Information.

Comparing the halogen bond donors **1** and **2**, it is noted that the nitrogen on the pyridine ring and the carboxylic acid functional groups have contrasting roles in the overall crystal structures. Whereas the carboxylic acid of **2** favoured dimerization *via* hydrogen

Table 2.2: Selected single-crystal X-ray crystallographic data for 1a,1d and 1e

compound	**1a**	**1d**	**1e**
empirical formula	$C_{27}H_{24}INPBr$	$C_{38}H_{28}I_2N_2PBr$	$C_{45}H_{39}IN_3OP_2Cl$
FW (g/mol)	600.25	877.30	862.08
crystal color	colourless	colourless	colourless
crystal size (mm)	0.50 x 0.30 x 0.20	0.625 x 0.347 x 0.308	0.100 x 0.100 x 0.100
crystal system	triclinic	tetragonal	monoclinic
crystal space group	P-1	P-4 2_1 m	P $2_1/c$
T (K)	200(2)	200(2)	200(2)
a (Å)	9.789(2)	15.2918(12)	24.52(2)
b (Å)	10.949(2)	15.2918(12)	19.724(16)
c (Å)	12.974(3)	7.5919(6)	17.107(14)
α (°)	67.041(9)	90	90
β (°)	86.447(10)	90	92.882(17)
γ (°)	76.089(9)	90	90
V(Å^3)	1242.0(5)	1775.3(3)	8263(12)
Z	2	2	8
R_1 (final)	0.0336	0.0403	0.400
wR_2 (final)	0.0568	0.0683	0.0768

bonding and formed continuous frameworks, the pyridine group of **1** favoured the formation of discrete halogen-bonded fragments. This is most clearly observed in structures **1a** and **1d**, while the continuous framework observed in **1e** is a result of the presence of a water molecule rather than the halogen bond donor or acceptor. Consequently, the halogen bond donor **2** may be a more versatile compound for engineering cocrystals, allowing for a more robust design of halogen bonded frameworks. Conversely, the basicity of the pyridine ring on **1** carries the benefits of self-assembly and the opportunity to form halide salts, which has also been mentioned in our previous report.[43]

^{13}C Solid-State NMR Spectroscopy

Shown in Figure 2.5 are the ^{13}C SSNMR spectra of the cocrystals and precursors studied herein. The spectra of **1** and **2** have been previously reported.[43, 44] The ^{13}C analysis yielded

Table 2.3: Selected single-crystal X-ray crystallographic data for 2b,2c, and 2e

compound	**2b**	**2c**	**2e**
empirical formula	$C_{39}H_{32}I_2O_4PBr$	$C_{41}H_{34}I_2O_4PBr$	$C_{47}H_{38}IN_2O_2P_2Cl$
FW (g/mol)	929.32	955.36	887.08
crystal color	colourless	colourless	colourless
crystal size (mm)	0.100 x 0.100 x 0.100	0.100 x 0.100 x 0.100	0.100 x 0.100 x 0.100
crystal system	monoclinic	orthorhombic	monoclinic
crystal space group	$P\ 2_1/n$	$P\ n\ m\ a$	$P\ 2_1/n$
T (K)	200(2)	200(2)	200(2)
a (Å)	10.3558(2)	15.2297(4)	14.3122(6)
b (Å)	12.1985(3)	25.4689(9)	19.2273(9)
c (Å)	29.0810(6)	10.0477(3)	16.2184(7)
α (°)	90	90	90
β (°)	92.4750(10)	90	109.8460(10)
γ (°)	90	90	90
V(Å^3)	3670.24(14)	3897.3(2)	4198.0(3)
Z	4	4	4
R_1 (final)	0.0354	0.0380	0.0402
wR_2 (final)	0.0625	0.0627	0.0812

sufficient signal within a few hours for each compound, offering a quantitative comparison of the chemical shifts for both the halogen bond donor and the cation relative to the pure starting materials. The chemical shifts of the carboxylic acid group (COOH), the acetylene carbon (C≡C-I), and the carbon covalently bonded to iodine (C-I) have been summarized in Table 2.4. Although a satisfactory signal was obtained for each spectrum, the carbon covalently bonded to iodine remained difficult to observe as a result of the breadth of the resonance, low signal intensity of the resonance, and spectral overlap from the cation in some cases. The signal intensity for the cocrystals in Figure 2.5 appears to be lower than that for the pure starting materials as a result of the higher intensity of the cation's ^{13}C signal. Overall, the chemical shift changes observed in Figure 2.5 support the occurrence of cocrystallization, while there is an absence of signal from any unreacted starting materials. Although solvent-based crystallizations were used to grow crystals suitable for single crystal X-ray diffraction, the compounds studied here by SSNMR were analyzed directly from the mechanochemical preparations. As a result, mechanochemical ball milling appears to be a reliable route towards these unique halogen bonded compounds, and its combination with NMR crystallography can accelerate the discovery of novel halogen-bonded materials.

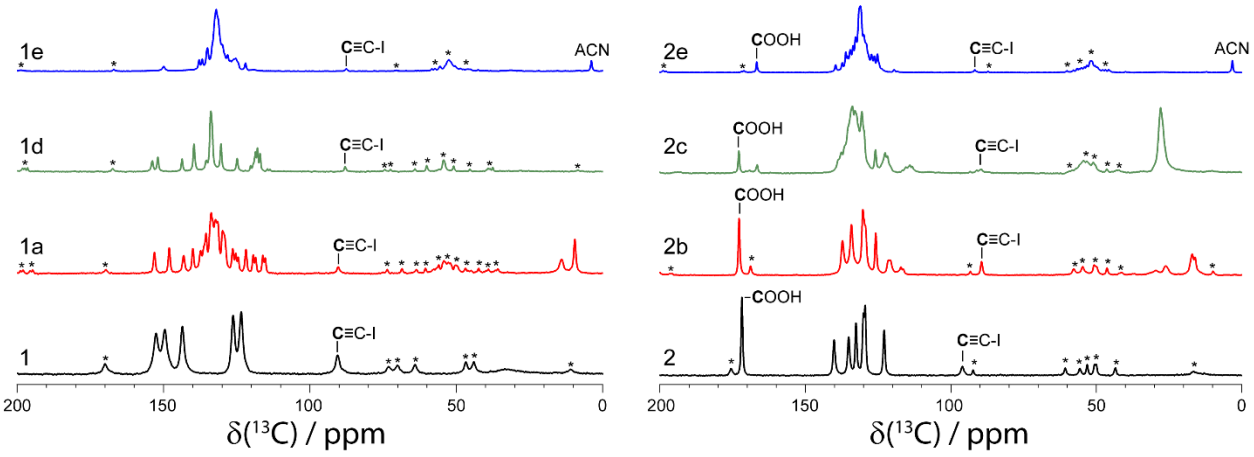

Figure 2.5: ^{13}C CP/MAS solid-state NMR spectra of the compounds investigated herein. The spectra of pure **1** and **2** were taken from previous reports.[43, 44] The labels denote the carboxylic acid (**C**OOH), acetylene (**C**≡C-I), and acetonitrile (ACN) carbons. The asterisks denote spinning sidebands (ν_{MAS} = 8 kHz).

Table 2.4: ^{13}C chemical shifts of the compounds studied herein

compound	XB moiety	δ(**C**OOH) / ppm	δ(**C**≡C-I) / ppm	δ(C-I) / ppm
1[i]	C-I···N	n/a	90.5 ± 0.5[i]	32.6 ± 1.1[i]
1a	C-I···Br$^-$	n/a	90.3 ± 0.2	[a]
1d	C-I···Br$^-$	n/a	87.9 ± 0.1	[a]
1e	C-I···Cl$^-$	n/a	87.5 ± 0.1	31.3 ± 1.2
2[i]	C-I···C≡C	171.7 ± 0.1[ii]	96.0 ± 0.1[ii]	14.9 ± 0.4[i]
2b	C-I···Br$^-$	172.7 ± 0.1	89.4 ± 0.1	[a]
2c	C-I···Br$^-$	172.8 ± 0.1	89.5 ± 0.8	[a]
2e	C-I···Cl$^-$	166.7 ± 0.1	91.7 ± 0.2	27.5 ± 2.3

[i] Chemical shifts of pure **1** and **2** have been reported elsewhere.[43, 44]
[a] Resonance not observed due to breadth and low signal-to-noise.

In comparison to their respective starting materials, the ^{13}C chemical shift of the acetylene carbon (C≡C-I) appears to be consistently lower in the cocrystals. For instance, there is a difference of 6.6 ± 0.1 ppm in the chemical shift of the acetylene carbon when comparing **2** to **2b**. Further, this decrease in the ^{13}C chemical shift is greater for cocrystals of **2** than for cocrystals of **1**. This may be a result of the starting material of **1** exhibiting a C-I···N halogen bond, while the starting material of **2** exhibits a weaker C-I···C≡C halogen bond coordinating the acetylene carbon. In contrast, the C-I chemical shift appears to increase when comparing **2** to **2e**, with a difference of 12.6 ± 2.3 ppm upon the formation of the cocrystals. This large increase contrasts with the comparison between **1** and **1e**, which saw an insignificant change in the chemical shift. This decrease in the ^{13}C chemical shift of the acetylene carbon and increase in the C-I carbon is in agreement with our previous reports for both compound **1** and compound **2**.[43, 44]

In regards to the ^{13}C resonance of the carboxylic acid of series **2**, the chemical shift appeared to be overall sensitive to the hydrogen bonding motif exhibited in the crystal structure. In the compounds featuring an O-H···O hydrogen bond dimerization, the chemical shifts did not significantly change, with a slight increase of 1.1 ± 0.1 ppm when comparing

2 to compound **2c**. However, upon the formation of a O-H···Cl^- hydrogen bond, a significant decrease of -5.0 ± 0.1 ppm is observed. As a result, the ^{13}C chemical shift of the carboxylic acid may be an indicator to the nature of hydrogen bonding motif in the crystal structure. This appears to be in agreement with our previous results, where the formation of a O-H···N hydrogen bonding motif featuring **2** and a nitrogen-containing heterocycle yielded a decrease in the ^{13}C resonance of the carboxylic acid on the order of 3 ppm.

^{31}P solid-state NMR spectroscopy. Due to its higher sensitivity compared to ^{13}C, ^{31}P SSNMR boasts the advantage of rapidly identifying excess starting material and the presence of side phases in mechanochemically prepared powders. Previously, ^{31}P SSNMR has been used to investigate pure phosphonium halide salts, in addition to halogen-bonded cocrystals featuring phosphonium selenides and oxides, showing clear chemical shift changes upon the occurrence of cocrystallization.[51–54] The compounds reported herein were explored by ^{31}P SSNMR after their preparation by mechanochemical ball milling without further manipulations; spectra are shown in Figure 2.6. The P chemical shifts of the halogen-bonded cocrystals were compared to chemical shifts of the pure halide salts, which can be found in Table 2.5. In these cases, there is a clear and unambiguous chemical shift difference between the pure phosphonium halide salts and their respective cocrystals, with each site in the asymmetric unit of the crystal structure having a unique chemical shift. Each spectrum required approximately 5 minutes to acquire.

The ^{31}P SSNMR spectra of compounds **1a**, **1d**, and **2b** each consist of a single resonance, with a chemical shift difference between the pure halide salt and the cocrystal of 2.9 ± 0.1 ppm for compound **1a**. The ^{31}P SSNMR spectrum of **1d** revealed trace ($< 10\%$) amounts of unreacted starting material remaining in the sample. The ^{31}P SSNMR spectrum of sample **2c** appears to have two resonances with a slight chemical shift difference of 0.8 ± 0.3 ppm. The presence of these two resonances could be due to the disorder present in the crystal structure, with the cyclopentyl group occupying the position of one of the phenyl groups.

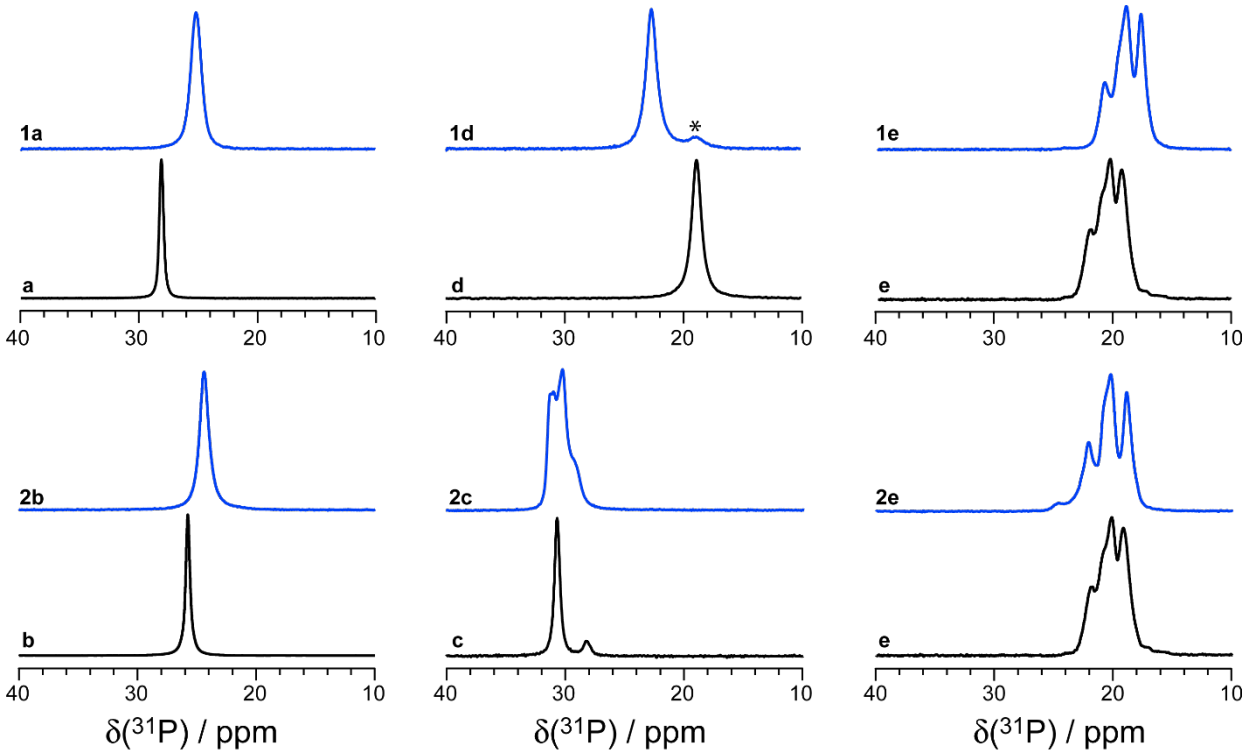

Figure 2.6: ^{31}P CP/MAS solid-state NMR spectra of the compounds investigated herein. The asterisks denote the presence of a trace residual impurity of pure **d** in the spectrum of **1d**.

Table 2.5: ^{31}P chemical shifts of compounds studied herein[a]

XB acceptor	$\delta(^{31}P)$ / ppm	cocrystal	$\delta(^{31}P)$ / ppm
a	28.1 ± 0.1	**1a**	25.2 ± 0.1
b	25.7 ± 0.1	**2b**	24.4 ± 0.1
c	30.7 ± 0.1	**2c**	31.1 ± 0.3
	28.2 ± 0.2		30.3 ± 0.1
d	18.8 ± 0.1	**1d**	22.6 ± 0.1

[a.] Chemical shifts are not reported for **e**, **1e**, and **2e** due to the presence of multiple crystallographic sites and residual dipolar coupling to ^{14}N.

The integration of both ^{31}P resonances reveals a ratio of approximately 0.56:0.44, which is in agreement with the occupancy ratio derived from the X-ray crystallography, which has a ratio of 0.568(9):0.432(9). The asymmetric broadening and splitting of the ^{31}P SSNMR spectrum of **e** suggests residual dipolar coupling between ^{31}P and the directly bonded ^{14}N atom. Although a published single-crystal X-ray structure of e indicates a single crystallographically distinct phosphorus site, the powder X-ray diffraction pattern of the sample used in our work does not match the pattern simulated based on the single-crystal structure (see Supporting Information). Our inability to simulate the[55] ^{31}P SSNMR spectrum based on a single ^{31}P site coupled to ^{14}N further suggests that the polymorph used in this work differs from the previously reported one. Nevertheless, resonance shifts upon cocrystallization are clear particularly for **1e** (Figure 2.6 and Figure S14).

Overall, ^{31}P SSNMR is a sensitive spectroscopic tool to identify the occurrence of cocrystallization. With experimental times on the order of 5 minutes, and the chemical shift sensitive to the crystallographic environment, ^{31}P offers several advantages to the crystal engineer. In contrast, the ^{13}C SSNMR required several hours to perform, and yields spectra with multiple resonances. As a result, the ^{13}C spectrum may be more ambiguous to interpret, especially with smaller chemical shift differences between the starting materials and the cocrystals. Nevertheless, ^{13}C SSNMR remains applicable to most organic compounds, while

^{31}P SSNMR obviously requires the presence of phosphorus in the sample.

2.5 Conclusions

The production of cocrystals of **1** and **2** with a series of halide salts was successfully performed by mechanochemistry, confirmed by both X-ray crystallography and multinuclear solid-state magnetic resonance spectroscopy. Across all six reported structures, a halogen bond has been observed between the iodine on the iodoacetylene group and the halide ion (Br^-, Cl^-). The cocrystals featuring **1** favoured discrete entities with the basic nitrogen on the pyridine ring acting as a hydrogen bond acceptor. In contrast, cocrystals built with **2** featured both hydrogen bonded dimers and C-I···X^- halogen bonds. The use of ^{31}P solid-state NMR allowed for a rapid confirmation for the occurrence of halogen bond-induced cocrystallization, while ^{13}C solid-state NMR was a reliable indicator for the occurrence of both halogen bonding and hydrogen bonding motifs.

Conflicts of Interest

There are no conflicts to declare.

Acknowledgements

PMJS and DLB thank the Natural Sciences and Engineering Research Council of Canada for a scholarship and for research funding, respectively.

Supporting Information Available

CIFs, powder X-ray diffractograms, further experimental details. For full diffraction datasets, refer to CCDC numbers 1909609 (**1a**), 1909624 (**1d**), 1909625 (**1e**), 1909626 (**2b**), 1909627 (**2c**), 1909628 (**2e**).

References

[1] S. Abe, H. Tabe, H. Ijiri, K. Yamashita, K. Hirata, K. Atsumi, T. Shimoi, M. Akai, H. Mori, S. Kitagawa, and T. Ueno *ACS Nano*, vol. 11, pp. 2410–2419, 2017.

[2] M. Lusi, "Cryst. growth des," vol. 18, pp. 3704–3712, 2018.

[3] M. Haque, A. Gandi, R. Mohanraman, Y. Weng, B. Davaasuren, A.-H. Emwas, C. Combe, D. Baran, A. Rothenberger, U. Schwingenschlögl, H. Alshareef, S. Dong, and T. Wu *Adv. Func. Mater.*, vol. 29, p. 1809166, 2019.

[4] T. Murata, C. Yamada, K. Furukawa, and Y. Morita *Communications Chemistry*, vol. 1, p. 47, 2018.

[5] C. Aakeröy, N. Champness, and C. Janiak *CrystEngComm*, vol. 12, pp. 22–43, 2010.

[6] G. Desiraju *Angew. Chem. Int. Ed. Engl*, vol. 34, pp. 2311–2327, 1995.

[7] E. Grothe, H. Meekes, E. Vlieg, J. Horst, and R. Gelder *Cryst. Growth Des*, vol. 16, pp. 3237–3243, 2016.

[8] S. e. a. Aitipamula *Cryst. Growth Des*, vol. 12, pp. 2147–2152, 2012.

[9] D. Weyna, T. Shattock, P. Vishweshwar, and M. Zaworotko *Cryst. Growth Des*, vol. 9, pp. 1106–1123, 2009.

[10] J.-L. Do and T. Friščić *SynLett*, vol. 28, pp. A–AA, 2017.

[11] G. Bowmaker *Chem. Commun*, vol. 49, pp. 334–348, 2013.

[12] P. Szell, S. Gabriel, E. Caron-Poulin, O. Jeannin, M. Fourmigué, and D. L. Bryce *Cryst. Growth Des*, vol. 18, pp. 6227–6238, 2018.

[13] A. Mukherjee, S. Tothadi, and G. Desiraju *Acc. Chem. Res*, vol. 47, pp. 2514–2524, 2014.

[14] C. Aakeröy, T. Wijethunga, and J. Desper *J. Mol. Struc*, vol. 1072, pp. 20–27, 2014.

[15] P. Metrangolo, H. Neukirch, T. Pilati, and G. Resnati *Acc. Chem. Res*, vol. 38, pp. 386–395, 2005.

[16] P. Politzer and J. Murray *Crystals*, vol. 7, pp. 212–226, 2017.

[17] T. Clark, M. Hennemann, J. Murray, and P. Politzer *J. Mol. Model*, vol. 13, pp. 291–296, 2007.

[18] P. Politzer, J. Murray, T. Clark, and G. Resnati *Phys. Chem. Chem. Phys*, vol. 19, pp. 32166–32178, 2017.

[19] G. Desiraju, P. Ho, L. Kloo, A. Legon, R. Marquardt, P. Metrangolo, P. Politzer, G. Resnati, and K. Rissanen *Pure Appl. Chem*, vol. 19, pp. 1711–1713, 2013.

[20] K. Riley, J. Murray, J. Fanfrlík, J. Řezáč., R. Solá, M. Concha, F. Ramos, and P. Politzer *J. Mol. Model*, vol. 17, pp. 3309–3318, 2011.

[21] K. Riley, J. Murray, J. Fanfrlík, J. Řezáč., R. Sola, M. Concha, F. Ramos, and P. Politzer *J. Mol. Model*, vol. 19, pp. 4651–4659, 2013.

[22] C. Aakeröy, T. Wijethunga, J. Desper, and M. Đaković *Cryst. Growth Des*, vol. 15, pp. 3853–3861, 2015.

[23] C. Aakeröy, D. Welideniya, and J. Desper *CrystEngComm*, vol. 19, pp. 11–13, 2017.

[24] L. González, N. Gimeno, R. Tejedor, V. Polo, M. Ros, S. Uriel, and J. Serrano *Chem. Mater*, vol. 25, pp. 4503–4510, 2013.

[25] H. Yamamoto, R. Maeda, J.-I. Yamaura, and R. Kato *J. Mater. Chem*, vol. 11, pp. 1034–1041, 2001.

[26] L. Turunen, F. Pan, N. Beyeh, J. Trant, R. Ras, and K. Rissanen *Cryst. Growth Des*, vol. 18, pp. 513–520, 2018.

[27] C. Gunawardana, M. Đaković, and C. Aakeröy *Chem. Commun*, vol. 54, pp. 607–610, 2018.

[28] C. Laurence, M. Queignec-Cabanetos, T. Dziembowska, R. Quiegnec, and B. Wojtkowiak *J. Am. Chem. Soc*, vol. 103, pp. 2567–2573, 1981.

[29] L. Luo, C. Wilhelm, A. Sun, C. Grey, J. Lauher, and N. Goro *J. Am. Chem. Soc*, vol. 130, pp. 7702–7709, 2008.

[30] C. Perkins, S. Libri, H. Adams, and L. Brammer *CrystEngComm*, vol. 14, pp. 3033–3038, 2012.

[31] N. Goroff, S. Curtis, J. Webb, F. Fowler, and J. Lauher *Org. Lett*, vol. 7, pp. 1891–1893, 2005.

[32] M. Fourmigué and A. Cryst *Acta Crystallogr*, vol. B73, pp. 138–139, 2017.

[33] J. Grebe, G. Geiseler, K. Harms, K. Dehnicke, and Z. Naturforsch *Z. Naturforsch*, vol. 54b, pp. 77–86, 1999.

[34] M. Pfrunder, A. Micallef, L. Rintoul, D. Arnold, and J. McMurtrie *Cryst. Growth Des*, vol. 16, pp. 681–695, 2016.

[35] J. Lieffrig, O. Jeannin, and M. Fourmigué *J. Am. Chem. Soc*, vol. 135, pp. 6200–6210, 2013.

[36] P. Szell, B. Gabidullin, and D. L. Bryce *Acta Crystallogr*, vol. B73, pp. 153–162, 2017.

[37] A. Brown and P. Beer *Chem. Commun*, vol. 52, pp. 8645–8658, 2016.

[38] J. Lim, I. Marques, V. Félix, and P. Beer *J. Am. Chem. Soc*, vol. 139, pp. 12228–12239, 2017.

[39] D. Cinčić, T. Friščić, and W. Jones *J. Am. Chem. Soc*, vol. 130, pp. 7524–7525, 2008.

[40] K. Lisac, V. Nemec, F. Topić, M. Arhangelskis, P. Hindle, R. Tran, I. Huskić, A. Morris, T. Friščić, and D. Cinčić *Cryst. Growth Des*, vol. 18, pp. 2387–2396, 2018.

[41] D. Cinčić, T. Friščić, and W. Jones *Chem. Eur. J*, vol. 14, pp. 747–753, 2008.

[42] Y. Xu, J. Viger-Gravel, I. Korobkov, and D. L. Bryce *J. Phys. Chem. C*, vol. 119, pp. 27104–27117, 2015.

[43] P. Szell, G. Cavallo, G. Terraneo, P. Metrangolo, B. Gabidullin, and D. L. Bryce *Chem. Eur. J*, vol. 24, pp. 11364–11376, 2018.

[44] P. Szell, J. Dragon, S. Zablotny, S. Harrigan, B. Gabidullin, and D. L. Bryce *New J. Chem*, vol. 42, pp. 10493–10501, 2018.

[45] *APEX 2.* Madison, Wisconsin, USA: Bruker AXS Inc, 2012.

[46] G. Sheldrick, *SADABS, Program for empirical absorption correction of area detector data.* Germany: University of Göttingen, 1996.

[47] G. Sheldrick *Acta Crystallogr*, vol. C71, pp. 3–8, 2015.

[48] L. Farrugia *J. Appl. Crystallogr*, vol. 32, pp. 837–838, 1999.

[49] L. Farrugia *J. Appl. Crystallogr*, vol. 45, pp. 849–854, 2012.

[50] A. Spek *Acta Crystallogr*, vol. D65, pp. 148–155, 2009.

[51] K. Burgess, I. Korobkov, and D. L. Bryce *Chem. Eur. J*, vol. 18, pp. 5748–5728, 2012.

[52] Y. Xu, L. Champion, B. Gabidullin, and D. L. Bryce *Chem. Commun*, vol. 53, pp. 9930–9933, 2017.

[53] J. Viger-Gravel, J. Meyer, I. Korobkov, and D. L. Bryce *CrystEngComm*, vol. 16, pp. 7285–7297, 2014.

[54] Y. Xu, J. Huang, B. Gabidullin, and D. L. Bryce *Chem. Commun*, vol. 54, pp. 11041–11043, 2018.

[55] C. Knapp and R. Uzun *Acta Crystallogr*, vol. E66, p. 3185, 2010.

Chapter 3

Nuclear Quadrupolar Resonance of Antimony Complexes

In the past decade, there has been increasing interest in the study of non covalent interactions such as halogen bonding. However, in recent years, the focus has shifted towards a variety of similar interactions such as pnictogen, chalcogen, tetrel, aerogen and triel bonds[1–6] All of these interactions are a type of sigma hole[7, 8] interaction between an electrophilic region on the atom which corresponds to the respective group and an electron-rich source such as a Lewis base. These interactions are known to have a central role in crystal engineering, catalyst, anion recognition and drug design.[9–12]

The pnictogen group has gained interest in the crystal engineering field due to recent studies that have revealed its role in the design of new structures. In some of these studies, it has been shown that the strength of the interaction is comparable to hydrogen bonding.[13] The electrostatic potential of pnictogen bonding increases as the size the atom increases (e.g. N, P, As, Sb, Bi). The depleted region interacts with an electron rich moiety such as a Lewis base. These interactions are highly regarded in the crystal engineering world due to to its predictability. To describe the interactions, we use the angle θ of the $R - Pn \cdots Y$ and the normalized bond length. The normalized bond length corresponds to the ratio between

the sum of the Van der Waals radii and the distance between the atoms. A value below 1 indicates the presence of electrostatic interactions. The angle of the bond is usually between 155 deg and 180 deg as shown in the figure3.1.

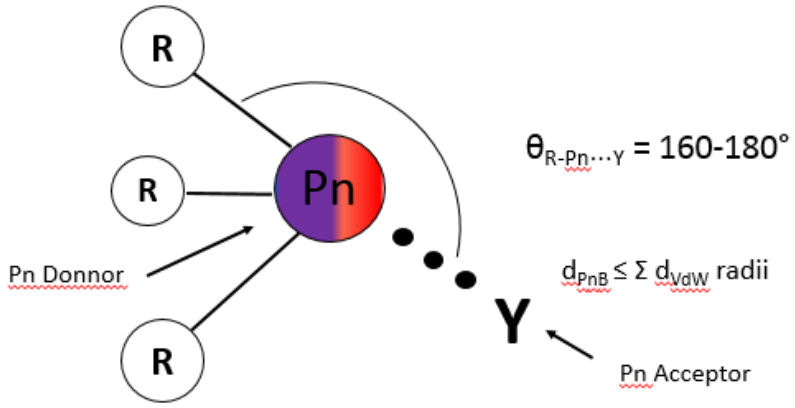

Figure 3.1: Visual representation of a pnictogen bond. Pn represents the pnictogen atom and R represents the electron withdrawing groups. The red portion signifies the positive electrostatic region on the pnictogen.

Solid-state nuclear magnetic resonance spectroscopy has been shown to be a powerful tool to provide insights in the characterization of halogen bonding interactions. This technique provides new perspective on the local bond geometry and the spectral parameters.[14, 15]

In the field of pnictogen bonds, the ones using antimony are the most known. Antimony has two NMR active isotopes which are both quadrupolar. The isotope ^{121}Sb has a spin quantum number of 5/2 and a natural abundance of 57.21%. The other isotope is ^{123}Sb has a spin quantum number of 7/2 and a relative abundance of 42.79%. The SSNMR study of antimony complexes are extremely limited due to the very large quadrupolar moment of antimony.[16] The quadrupole moment of antimony interacts with the electric field gradient tensor around the nucleus and this creates the quadrupolar interaction (QI). There are two components that describe the QI: the quadrupolar coupling constant (Cq), electric field gradient tensor (EFG) asymmetry parameter (η) as explained in section 1.3.8.

Despite the challenges regarding the antimony SSNMR spectroscopy our group, as well as other researchers around the world namely Cozzolino[17] and Friščić[18] , continues to investigate

the use of antimony in different applications. Nuclear quadrupolar resonance spectroscopy (NQR) is an effective way to gather information on hard to observe nuclei due to large quadrupolar interactions. NQR is performed without any magnetic field, and the signal emerges from the QI. The signals acquired can be viewed as the frequency between the energy levels. As a reminder, the energy levels of a quadrupolar nuclei in the absence of a magnetic field are degenerate (e.g $\pm\frac{1}{2} \rightarrow \pm\frac{3}{2}$ and $\pm\frac{3}{2} \rightarrow \pm\frac{5}{2}$).

This section is a collaborative work with two different institutions. The first collaboration is with Professor Anthony Cozzolino from Texas Tech University. The second collaboration is with Professor Tomislav Friščić from McGill University. This chapter will describe my contribution to these collaborations and the results that were obtained.

3.1 Texas Tech University Collaboration

In this first collaboration, we looked at three different cocrystals made from the same antimony complex. These cocrystals have a pnictogen bonding interaction between the antimony atom and the different pnitogen bond donor. I was in charge of conducting nuclear quadrupolar resonance spectroscopy (NQR) on the compound provided by Professor Cozzolino and his group to evaluate the electrostatic interaction. The cocrystals provided by Professor Cozzolino's group are shown in the figure below3.2.

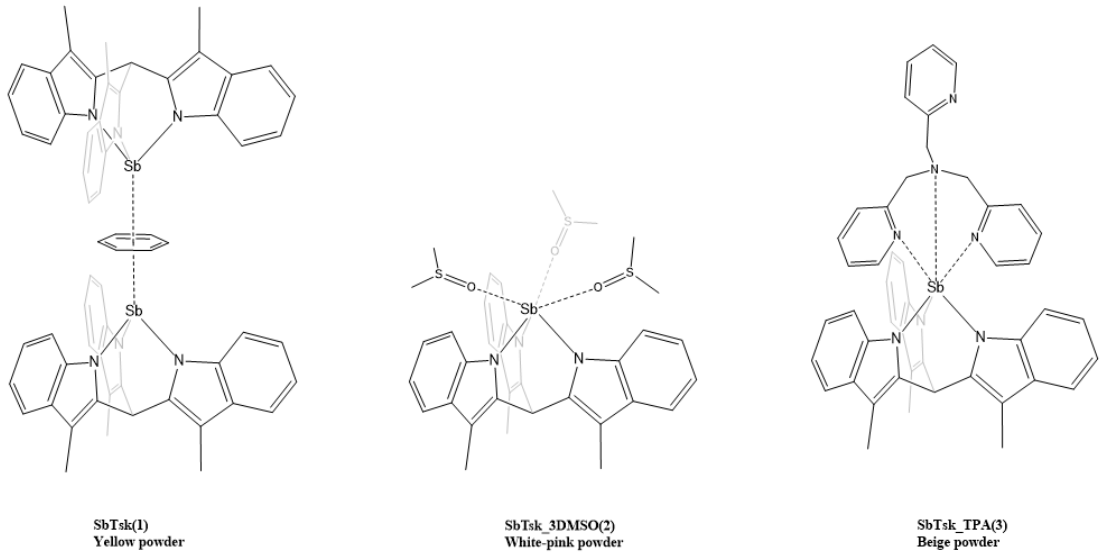

Figure 3.2: Compounds given by Professor Cozzolino's team

The first compound consists of two antimony complex synthesis by Cozzolino's group that interacts with the pi electrons of a benzene ring, as shown in figure 3.2. The second structure consists of the same antimony complex which interacts with three dimethyl sulfoxides (DMSO). The last structure consists of the antimony complex that interacts with Tris(2-pyridylmethyl)amine (TPA).

3.1.1 Experimental Analysis

The experimental analysis was performed following this procedure. Lower NQR frequencies were acquired using a Bruker Avance III 200 NMR console with a static 5 mm XY probe. Higher NQR frequencies were acquired using a Bruker Avance III 400 NMR console with a home built probe. All data was acquired at liquid nitrogen temperature and without any applied magnetic field. A Hahn-echo pulse sequence ($\pi/2$-τ-π-τ) was used with pulse lengths of 4 and 8 μs and a recycle delay of 0.2 s. The total number of transients for each signal was 1024.[19, 20]

3.1.2 Computational Analysis

The computational work was performed by Dr. Patrick Szell using these parameters. All calculations were performed using ADF2018[21, 22] software. Cluster models were prepared with GaussView[23] using the respective crystal structures, including all molecules interacting with the antimony atom via pnictogen bonding (e.g., benzene, DMSO, or TPA). All atomic coordinates were initially optimized using the revPBE functional with the TZP basis set while constraining the atoms covalently bonded to antimony and the chalcogen bond acceptor atoms. The antimony atom and the covalently bonded nitrogen atoms were subsequently optimized using the TZ2P basis set, accounting for relativistic effects using ZORA.[24] The pnictogen bond acceptor atoms (O from DMSO, C from benzene, N from TPA) were fixed throughout all the geometry optimization cycles to prevent deviations from the crystal structure. The EFG tensor was calculated on the optimized models using the revPBE functional with the TZ2P basis set, using ZORA relativistic corrections.[24] The output file was interpreted using EFG[25] Shield and the simulated NQR spectra were generated using QUEST.[26]

3.1.3 Results and Discussion

The result of the analysis shows that the synthesized compound interacts very differently with the surrounding which indicates the presence of a pnictogen bonding interaction. As shown in table 3.1 below and in the figures 3.3,3.4, the quadrupolar coupling constant (Cq) and the asymmetry parameter (η) are different for all of the compounds.

Table 3.1: Experimental and DFT calculated ^{121}Sb quadrupolar coupling parameters and associated NQR frequencies.

Sample	$\nu_1(^{121}Sb)/MHz$		$\nu_2(^{121}Sb)/MHz$		$C_Q(^{121}Sb)/MHz$		η	
	Exp.	Calc.	Exp.	Calc.	Exp.	Calc.	Exp.	Calc.
SbTsk(1)	83.21±0.01	78.7	166.40±0.01	157.2	554.71±0.07	524.5	0.005±0.001	0.002
SbTsk_3DMSO(2)	87.36±0.02	79.0	173.21±0.01	157.6	578.08±0.13	526.4	0.079±0.001	0.029
SbTsk_TPA(3)	88.78±0.01	75.8	175.90±0.01	150.9	587.25±0.06	504.3	0.036±0.001	0.045

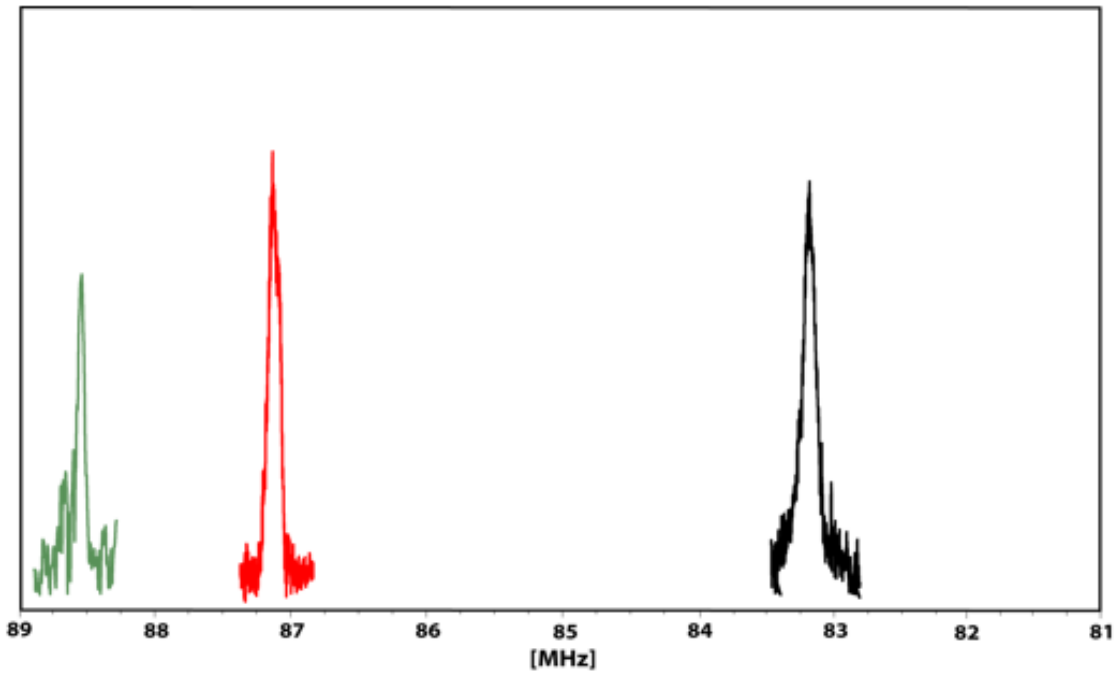

Figure 3.3: Pure ^{121}Sb NQR experimental spectra (ν_1) of 1-benzene (black), 2-DMSO (red) and 3-TPA (green)

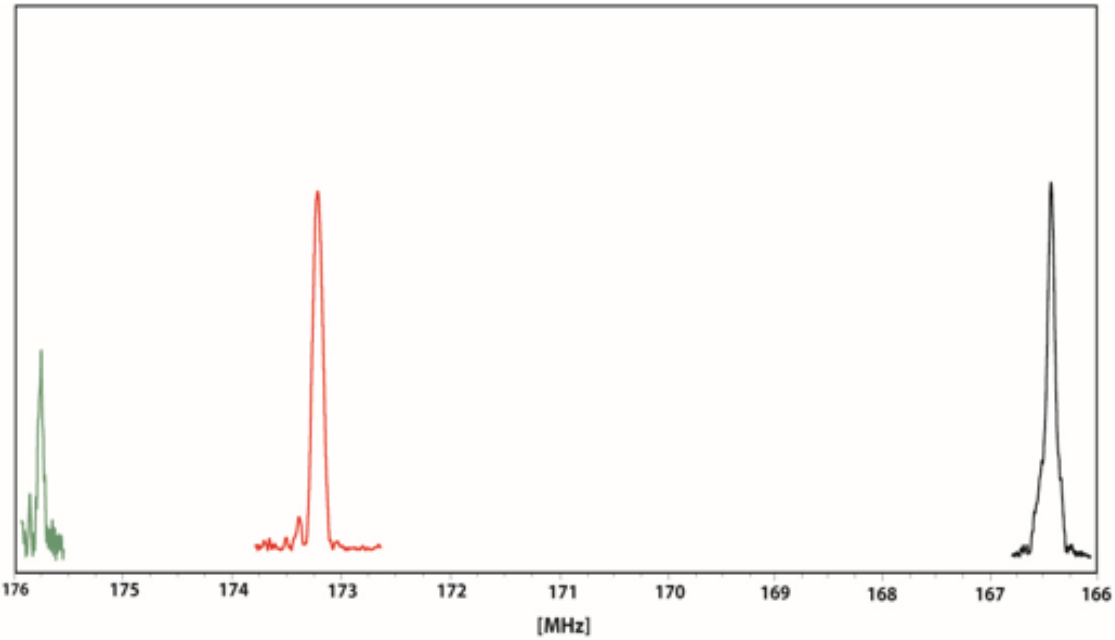

Figure 3.4: Pure ^{121}Sb NQR experimental spectra (ν_2) of 1-benzene (black), 2-DMSO (red) and 3-TPA (green)

Table 3.2: Pnictogen bond geometry of the compounds made by Professor Cozzolino's group

compound	PnB moiety	PnB length ($d_{I\cdots Y}$) / Å	R_{PnB} [a]	PnB angle $\theta_{N-Sb\cdots Y}$ (°)
SbTsk(1)	$N-Sb\cdots C$	3.648	N/A	127.45
SbTsk_3DMSO(2)	$N-Sb\cdots O$	2.675	0.74	156.76
		2.651	0.74	152.81
		2.631	0.73	161.28
SbTsk_TPA(3)	$N-Sb\cdots N$	2.754	0.71	165.10
		2.614	0.72	157.51
		3.330	0.92	140.34

[a] The normalized distance parameter was calculated using $R_{PnB} = \frac{dI\cdots Y}{\Sigma d_{VdW}}$ where Σd_{VdW} is denoted the sum of the Van der Waals radii.

Looking at the C_Q values, we see that the SbTsk_benzene cocrystal has the lowest experimental value (554.71 MHz), but we cannot calculate the normalized distance parameter between the antimony and the center of the benzene ring due to the unability to deternine the Van der Waals radii at the center of the ring. We can assume that there is a weak pnictogen bonding due to the way the crystal structure is held together. For the SbTsk_3DMSO cocrystal, the C_Q value is 578.08 MHz and when looking at the R_{PnB}, we notice that the values for each oxygen atom vary from 0.73 to 0.74 and the angle varies from 152.81 to 161.10 which indicates the presence of a strong electrostatic interaction and a symmetrical environment. The SbTsk_TPA cocrystal has the highest C_Q with a value of 587.25 MHz and a R_{PnB} range of 0.71 to 0.92 and angles ranging from 140.34 to 165.10. Since the R_{PnB} values are lower than 1, it indicates a pnictogen bonding interaction. However, The large variation of bond lengths and bond angles suggest that these pnictogen bonding interactions are asymmetric. When comparing the quadrupole coupling constant of both TPA and DMSO compounds, we observe a considerable difference which might be due to the DMSO increasing the symmetry around the antimony atom and the decreasing the anisotropy, whereas the TPA has a less symmetrical environment around the antimony atom. The computational analyses the these complexes does not match exactly the trend observed in the experimental section shown in table 3.1 where the C_Q decreases as the symmetry of the molecule increases. The computational analysis results show a lower C_Q value for the TPA even though this

molecule has a lower symmetry. It might be important to rerun the calculation with different parameters to try to match the trend as best as possible. Since the initial compound was not provided, the analysis is incomplete. The only conclusion possible will be provided by comparing the three compounds together.

3.2 McGill University Collaboration

In this second collaboration, Professor Friščić and his research team sent the two compounds shown below. Both of these cocrystals are made from the same initial compound which is triphenylstibine. The first one is a cocrystal of triphenylstibine and 1,3,5-Triodotrifluorobenzene. This compound contains a halogen bond interaction between the iodine and the antimony as shown below in figure 3.5. The second one is a cocrystal made from triphenylstibine and 1,4-Diiodotetrafluorobenzene. This compound has no halogen bonded interaction. The interaction is between the pi electron of one of the phenyl group and the 1,4-Diiodotetrafluorobenzene as shown below in figure 3.5.

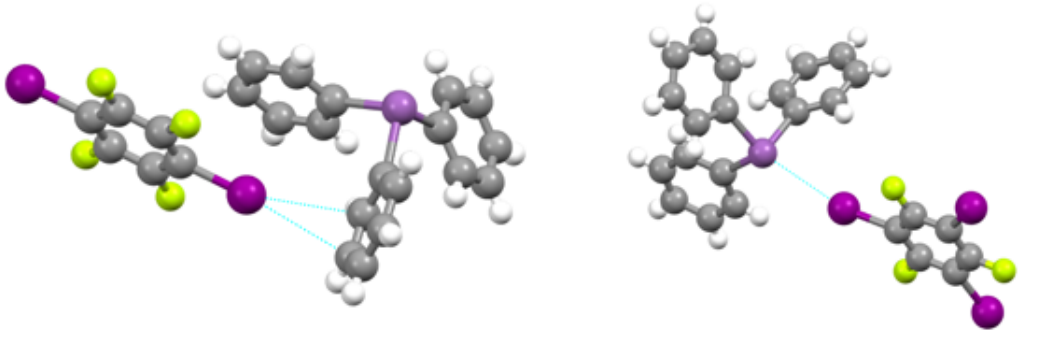

Figure 3.5: Crystal structure provided by Professor Friščić's research group

3.2.1 Experimental Analysis

The experimental analysis was performed following this procedure. Lower NQR frequencies were acquired using a Bruker Avance III 200 NMR console with a static 5 mm XY probe. Higher NQR frequencies were acquired using a Bruker Avance III 400 NMR console with a static 5mm x probe. All data was acquired at room temperature and without any applied magnetic field. A Hahn-echo pulse sequence ($\pi/2$-τ-π-τ) was used with pulse lengths of 4 and 8 μs and a recycle delay of 0.2 s. The total number of transients for each signal was 1024.[19, 20]

3.2.2 Computational Analysis

The computational calculations were performed by Tamali Nag using the following method. All calculations were performed using ADF2019 and ADF 2019.305[21, 22] software. Cluster models were prepared with GaussView4.1[23] using the respective crystal structures, including all molecules interacting with the antimony atom via halogen bonding (e.g., 1,3,5-Triiodotrifluorobenzene). All atomic coordinates were initially optimized using the revPBE functional with the TZ2P basis set while constraining the atoms covalently bonded to antimony and the halogen bond acceptor atoms. The antimony atom and the covalently bonded nitrogen atoms were subsequently optimized using the TZ2P basis set, accounting for relativistic effects using ZORA.[24] The halogen bond acceptor atoms (Sb from triphenylstibine) were fixed throughout all the geometry optimization cycles to prevent deviations from the crystal structure. The EFG tensor was calculated on the unoptimized and optimized models out of which the unoptimized models yielded a better match with the experimental results using the revPBE functional with the QZ4P basis set, using ZORA relativistic corrections.[24] The output file was interpreted using both EFGShield[25] and manual calculations. The simulated NQR spectra were generated using QUEST.[26]

3.2.3 Results and Discussion

Looking at the Cq and η values of the compound number 2, we see that it is lower than the initial compound which seems to match with the computational value as shown below Table 3.3. Usually, introducing an interaction like a halogen bond interaction will give more symmetry around the antimony nuclei which results in a lower Cq value for antimony. The presence of a halogen bond can be seen also by looking at the distance between the iodine and the antimony and dividing this value by the sum of their Van der Waals radii, as shown below Table 3.4. Contrary the compound number 1, the Cq value has increased. This is due to the the way the 1-4 diiodotetrafluorobenzene interacts with the antimony compound. In the case of compound 1, it interacts with one of the phenyl groups on the antimony compound which acts as an electron withdrawing group and will ultimately negatively change the EFG around the nucleus.

Table 3.3: Experimental and DFT calculated ^{121}Sb quadrupolar coupling parameters and associated NQR frequencies.

Sample	$\nu_1(^{121}Sb)/MHz$		$\nu_2(^{121}Sb)/MHz$		$C_Q(^{121}Sb)/MHz$		η	
	Exp.	Calc.	Exp.	Calc.	Exp.	Calc.	Exp.	Calc.
Triphenylstibine	76.66±0.01	72.02	153.17±0.01	144.53	510.21	482.64	0.039±0.001	0.034
1	77.01±0.02	73.11	153.91±0.01	145.62	513.13	486.89	0.024±0.001	0.035
2	71.94±0.01	66.57	143.54±0.01	133.08	478.65	444.82	0.042±0.001	0.024

Table 3.4: Halogen bond geometry of the compounds made by Professor Friščić's group

compound	XB moiety	XB length ($d_{I\cdots Y}$) / Å	R_{XB} [a]	XB angle $\theta_{C-I\cdots Y}$ (°)
1	N/A	N/A	N/A	N/A
2	C-I···Sb	3.575	0.88	168.28

[a] The normalized distance parameter was calculated using $R_{XB} = \frac{dI\cdots Y}{\Sigma d_{VdW}}$ where Σd_{VdW} is denoted the sum of the Van der Waals radii.

In conclusion, after NQR and computational analysis of the compound of Professor Friščić's research group, the compound number 2 contains a halogen bonding interaction. We confirm this analysis by looking at the experimental and computational quadrupolar coupling constant results and comparing them to the pure antimony complex, which is triphenylstibine. We can further confirm the presence of electrostatic interactions by looking at the crystallographic parameters such as the bond angle and the normalized distance. The compound number 1 does not contain any σ-hole type of interaction, it contains only a pi bond interaction when looking at the crystallographic structure and also at the quadrupolar coupling constant which increases compared to the initial compound. One other way we could further confirm the presence of the halogen bonding interaction between the iodine and the antimony would be by computational analysis and NQR spectroscopy of iodine.

References

[1] G. Sánchez-Sanz, C. Trujillo, M. Solimannejad, I. Alkorta, and J. Elguero, "Orthogonal interactions between nitryl derivatives and electron donors: pnictogen bonds," *Phys. Chem. Chem. Phys.*, vol. 15, pp. 14310–14318, 2013.

[2] E. Alikhani, F. Fuster, B. Madebene, and S. J. Grabowski, "Topological reaction sites – very strong chalcogen bonds," *Phys. Chem. Chem. Phys.*, vol. 16, pp. 2430–2442, 2014.

[3] Q. Li, X. Guo, X. Yang, W. Li, J. Cheng, and H.-B. Li, "A σ-hole interaction with radical species as electron donors: does single-electron tetrel bonding exist?," *Phys. Chem. Chem. Phys.*, vol. 16, pp. 11617–11625, 2014.

[4] M. Marín-Luna, I. Alkorta, and J. Elguero, "Cooperativity in Tetrel Bonds," *The Journal of Physical Chemistry A*, vol. 120, no. 4, pp. 648–656, 2016.

[5] A. Bauzá and A. Frontera, "Aerogen Bonding Interaction: A New Supramolecular Force?," *Angewandte Chemie International Edition*, vol. 54, no. 25, pp. 7340–7343, 2015.

[6] E. C. Escudero-Adán, A. Bauzá, C. Lecomte, A. Frontera, and P. Ballester, "Boron triel bonding: a weak electrostatic interaction lacking electron-density descriptors," *Phys. Chem. Chem. Phys.*, vol. 20, pp. 24192–24200, 2018.

[7] T. Clark, M. Hennemann, J. S. Murray, and P. Politzer, "Halogen bonding: the σ-hole," *Journal of Molecular Modeling*, vol. 13, pp. 291–296, 2007.

[8] B. V. Pandiyan, P. Deepa, and P. Kolandaivel, "Studies on the σ-hole bonds (halogen, chalcogen, pnicogen and carbon bonds) based on the orientation of crystal structure," *Molecular Physics*, vol. 114, no. 24, pp. 3629–3642, 2016.

[9] S. Benz, A. I. Poblador-Bahamonde, N. Low-Ders, and S. Matile, "Catalysis with Pnictogen, Chalcogen, and Halogen Bonds," *Angewandte Chemie International Edition*, vol. 57, no. 19, pp. 5408–5412, 2018.

[10] J. Y. Lim and P. D. Beer, "Sigma-Hole Interactions in Anion Recognition," *Chem*, vol. 4, no. 4, pp. 731 – 783, 2018.

[11] M. Iwaoka, S. Takemoto, and S. Tomoda, "Statistical and Theoretical Investigations on the Directionality of Nonbonded S $\cdots$ O Interactions. Implications for Molecular Design and Protein Engineering," *Journal of the American Chemical Society*, vol. 124, no. 35, pp. 10613–10620, 2002.

[12] K. T. Mahmudov, M. N. Kopylovich, M. F. C. Guedes da Silva, and A. J. L. Pombeiro, "Chalcogen bonding in synthesis, catalysis and design of materials," *Dalton Trans.*, vol. 46, pp. 10121–10138, 2017.

[13] S. Zahn, R. Frank, E. Hey-Hawkins, and B. Kirchner, "Pnicogen Bonds: A New Molecular Linker?," *Chemistry – A European Journal*, vol. 17, no. 22, pp. 6034–6038, 2011.

[14] P. M. J. Szell, B. Gabidullin, and D. L. Bryce, "1,3,5-Tri(iodoethynyl)-2,4,6-trifluorobenzene: halogen-bonded frameworks and NMR spectroscopic analysis," *Acta Crystallographica Section B*, vol. 73, no. 2, pp. 153–162, 2017.

[15] P. M. J. Szell and D. L. Bryce, *Solid-State NMR Studies of Halogen Bonding*. Cham: Springer International Publishing, 2016.

[16] P. Pyykkö, "Year-2017 nuclear quadrupole moments," *Molecular Physics*, vol. 116, no. 10, pp. 1328–1338, 2018.

[17] S. Moaven, J. Yu, M. Vega, D. K. Unruh, and A. F. Cozzolino, "Self-assembled reversed bilayers directed by pnictogen bonding to form vesicles in solution," *Chem. Commun.*, vol. 54, pp. 8849–8852, 2018.

[18] K. Lisac, F. Topić, S. C. Arhangelskis, P. A. Julien, C. W. Nickels, A. J. Morris, T. Friščić, and D. Cinčić, "Halogen-bonded cocrystallization with phosphorus, arsenic and antimony acceptors," *Nature Communication*, vol. 10, 2019.

[19] C. Leroy, R. Johannson, and D. L. Bryce, "$^{121/123}$Sb Nuclear Quadrupole Resonance Spectroscopy: Characterization of Non-Covalent Pnictogen Bonds and NQR Crystallography," *The Journal of Physical Chemistry A*, vol. 123, no. 5, pp. 1030–1043, 2019.

[20] P. M. J. Szell, L. Grébert, and D. L. Bryce, "Rapid Identification of Halogen Bonds in Co-Crystalline Powders via ^{127}I Nuclear Quadrupole Resonance Spectroscopy," *Angewandte Chemie International Edition*, vol. 58, no. 38, pp. 13479–13485.

[21] G. te Velde, F. M. Bickelhaupt, E. J. Baerends, C. Fonseca Guerra, S. J. A. van Gisbergen, J. G. Snijders, and T. Ziegler, "Chemistry with ADF," *Journal of Computational Chemistry*, vol. 22, no. 9, pp. 931–967, 2001.

[22] C. Fonseca Guerra, J. Snijders, G. te Velde, and et al., "Towards an order-N DFT method," *Theor Chem Acc*, vol. 99, p. 391–403, 1998.

[23] R. Dennington, T. Keith, and J. Millam, "Gauss View, Version 5," *Semichem Inc., Shawnee Mission.*, 2009.

[24] E. van Lenthe, A. Ehlers, and E.-J. Baerends, "Geometry optimizations in the zero order regular approximation for relativistic effects," *The Journal of Chemical Physics*, vol. 110, no. 18, pp. 8943–8953, 1999.

[25] S. Adiga, D. Aebi, and D. L. Bryce, "EFGShield — A program for parsing and summarizing the results of electric field gradient and nuclear magnetic shielding tensor calculations," *Canadian Journal of Chemistry*, vol. 85, no. 7-8, pp. 496–505, 2007.

[26] F. A. Perras, C. M. Widdifield, and D. L. Bryce, "QUEST—QUadrupolar Exact SofTware: A fast graphical program for the exact simulation of NMR and NQR spectra for quadrupolar nuclei," *Solid State Nuclear Magnetic Resonance*, vol. 45-46, pp. 36 – 44, 2012.

Chapter 4

Conclusion

4.1 General Conclusion

The halogen bonding interaction, along with other σ-hole interactions, has been experiencing a rise in interest over the last decades. This rise of interest of these types of interactions is due to the high tunability and predictability caused by the linearity of the interaction. It has gained a lot of interest in the crystal engineering world and also in some pharmaceutical applications. The halogen bond can be divided in two components: the halogen bond donor, which contains the halogen, and the acceptor which contains the electron rich source. In this thesis, we analyzed the σ-hole interaction through different means. In chapter 2, we looked at mechanochemistry to create new halogen bonded cocrystals and how we can use mechanochemistry to quickly and repeatedly create halogen bonded cocrystals. We analyzed these newly formed interactions with solid-state nuclear magnetic resonance spectroscopy and X-ray diffraction. We performed ^{13}C and ^{31}P cross polarization experiments and single crystal X-ray and powder X-ray diffraction experiments. ^{31}P SSNMR experiment has shown to be a rapid way to assess the presence of a halogen bond while ^{13}C SSNMR is more time consuming, but it also revealed the presence of halogen bonds and hydrogen bonds. Single crystal X-ray diffraction was used to measure the angle and the distance between the halogen

bond donor and acceptor while powder X-ray diffraction was used to confirm if the cocrystal formed was the right polymorph.

In the second part of the thesis, we looked at non-covalent interactions involving the pnictogen group. Pnictogen bonding, along with other σ-hole interactions, is at the forefront of the crystal engineering field and drug design. Due to the high demand of research in this field, new approaches of studying the interaction are needed. X-ray diffraction is a proven method to analyze the bond angle and distance but it does not give information on the interaction between the atoms. Since halogen and pnictogen atoms are mostly quadrupolar, with the exception of phosphorus and fluorine, performing solid-state nuclear magnetic resonance spectroscopy on these nuclei can be challenging due to their large quadrupolar moment. In the case where the quadrupolar interaction is too high and SSNMR spectroscopy is nearly impossible, nuclear quadrupolar resonance spectroscopy (NQR) is a viable option to gain information on the nuclei of interest. NQR is performed without an external magnetic field and gives information on the quadrupolar coupling constant Cq and the asymmetry parameter η.

In the first part of this section, I performed NQR analyses on three pnictogen bonded cocrystal. These three cocrystals are based on the same antimony complex cocrystalized with three pnictogen bond donors. The outcome of the NQR and computational analysis show that the antimony complex cocrystalized with a benzene ring provides a lower C_Q value but since we are unable to calculate the Van der Waals radii at the center of the benzene ring, we cannot calculate the normalized bond distance parameter and determine the strength of the interaction. The TPA and DMSO cocrystals have pnictogen bonding interactions and NQR analyses shows that the DMSO complex has the lowest C_Q value which is due to the more symmetrical environment around the nucleus. Since the initial compound was not provided for comparison, it is difficult to have a definitive conclusion on the overall interaction.

In the second section of this chapter, we looked at two different cocrystals made with

triphenylstibine. The first cocrystal exibits a halogen bonding interaction between 1,3,5-Triiodotrifluorobenzene (2), while the second cocrystal made from 1,4-Diiodetetrafluorobenzene (1) has a pi bond interaction between the phenyl group. When compared, the calculated and experimental quadrupole coupling constants for the cocrystal 2 are lower than the antimony initial compound which indicates a halogen bonding interaction. The second cocystal has a higher Cq than the initial compound, which corresponds to a change of the asymmetry parameter in the electric field gradient tensor around the nucleus. All in all, NQR spectroscopy is a useful complement to the spectroscopy's tool box.

4.2 Future Work

Another work that can be done in the first section would be to reuse the halogen bond donors (3IEP and 3IEBA) and make them cocrystalize with a series of acceptors such as pyridine N-oxide using the mechanochemistry techniques and evaluate the electrostatic interactions with different techniques such as SCXRD and ^{127}I NQR and ^{17}O labeld SSNMR. The purpose of this study would be to compare how N-oxydes and phosphonium salts interact with the halogen bond donors versus and help us gain information from a crystal engineering point of view.

For the Texas Tech Universty collaboration, one way we could expand the projects would be to use the pnictogen bond donor and make it crystallize with a series of acceptors containing ^{17}O labelled carboxylic acid such as terephtalic acid, trimesic acid and 9,10-Anthracenedicarboxylic acid. We could probe the electrostatic interaction with ^{121}Sb NQR and computational chemistry and also with ^{17}O SSNMR

In the collaboration with Professor Friščić, other experiments that could be performed in order to gain additional information on these halogen bonded and pi bonded cocrystals, would be to look at the ^{19}F SSNMR and ^{127}I NQR coupled with computational analyses. By performing ^{19}F SSNMR, we could gain information on the intensity of the pi bonding

interaction. Also, ^{127}I NQR analysis could be used confirm the previous NQR study.

Appendix A

Supporting Information

Mechanochemical Preparations of Anion Coordinated Architectures Based on 3-iodoethynylpyridine and 3-iodoethynylbenzoic Acid

Vincent M. Morin, Patrick M.J. Szell, Estelle Caron-Poulin, Bulat Gabidullin, and David L. Bryce* Chemistry Open, 2019, 8, 1328-1336

*Author to whom correspondence may be addressed

Department of Chemistry and Biomolecular Sciences

University of Ottawa

10 Marie Curie Private

Ottawa, Ontario K1N 6N5

Canada

Tel: +1-613-562-5800 ext.2018; fax: +1-613-562-5170

Email: dbryce@uottawa.ca

A.1 Experimental Masses and ^{13}C Solid-State NMR Parameters

Table A.1: Experimental masses and yields for the preparation of each cocrystal by ball milling, along with their respective melting points.

compound	mass 1 or 2 / mg (±2)	mass acceptor / mg (±2)	mass product / mg (±2)	yield (%)	stoichiometric ratio	melting point (deg C)
1a	132.0	182.9	299.1	95	1:1	122 – 124
1d	117.5	193.3	294.6	95	1:1	138 – 140
1e	85.8	215.0	68.3	23	1:1	78 – 82
2b	172.4	123.6	257.6	87	2:1	132 – 136
2c	73.0	227.1	234.4	78	1:2	118 – 122
2e	96.0	203.0	118.4	39	1:1	68 – 72

Table A.2: Selected ^{13}C solid-state NMR acquisition parameters for the samples obtained by slow evaporation and ball milling.

sample	spinning speeds	recycle delay (s)	number of transients
1a	8 kHz	10	1024
1d	8 kHz	10	1024
1e	8 kHz	10	2048
2b	8 kHz	10	1696
2b	8 kHz	10	1024
2e	8 kHz	10	1024

A.2 Powder X-ray Diffractograms

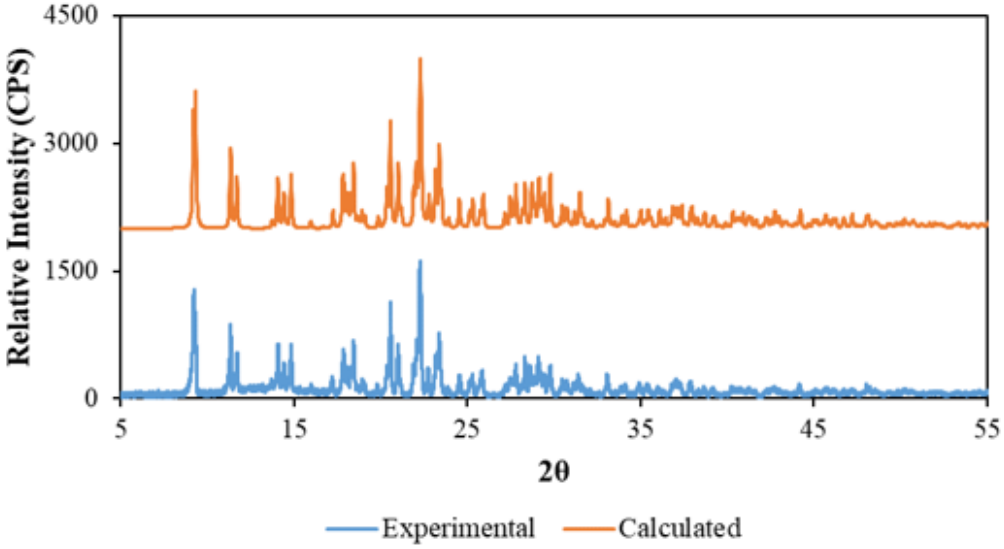

Figure A.1: Experimental and calculated powder X-ray diffractograms of **1a**, (3-iodoethynylpyridine) (ethyltriphenylphosphonium bromide).

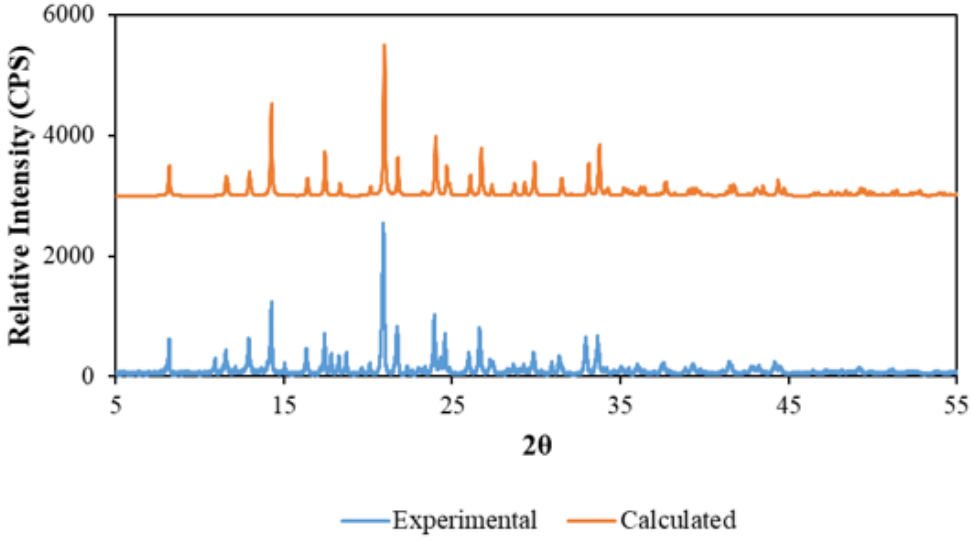

Figure A.2: Experimental and calculated powder X-ray diffractograms of **1d**, (3-iodoethynylpyridine) (tetraphenylphosphonium bromide).

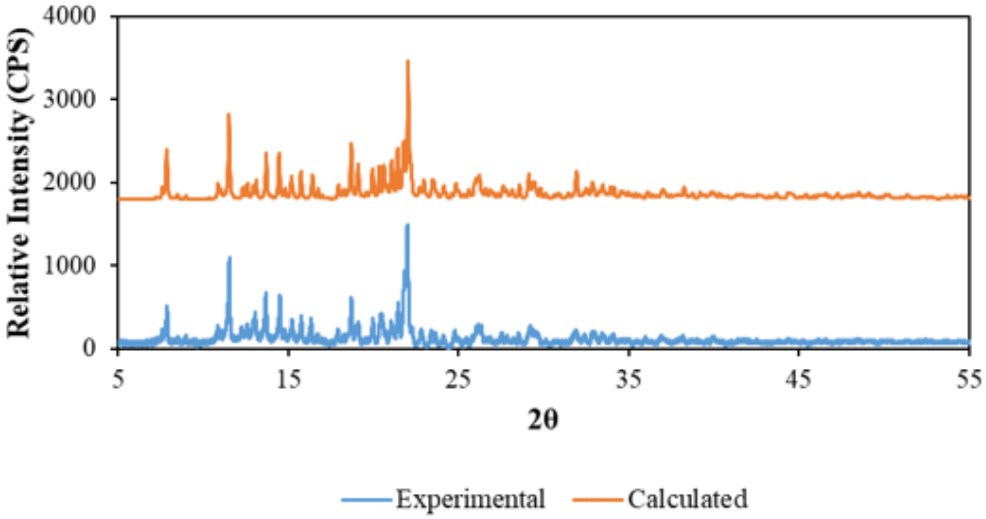

Figure A.3: Experimental and calculated powder X-ray diffractograms of **1e**, (3-iodoethynylpyridine)$_2$ (bis[triphenylphosphoranylidene] ammonium chloride)$_2$(H_2O)$_2$ (ACN)$_2$.

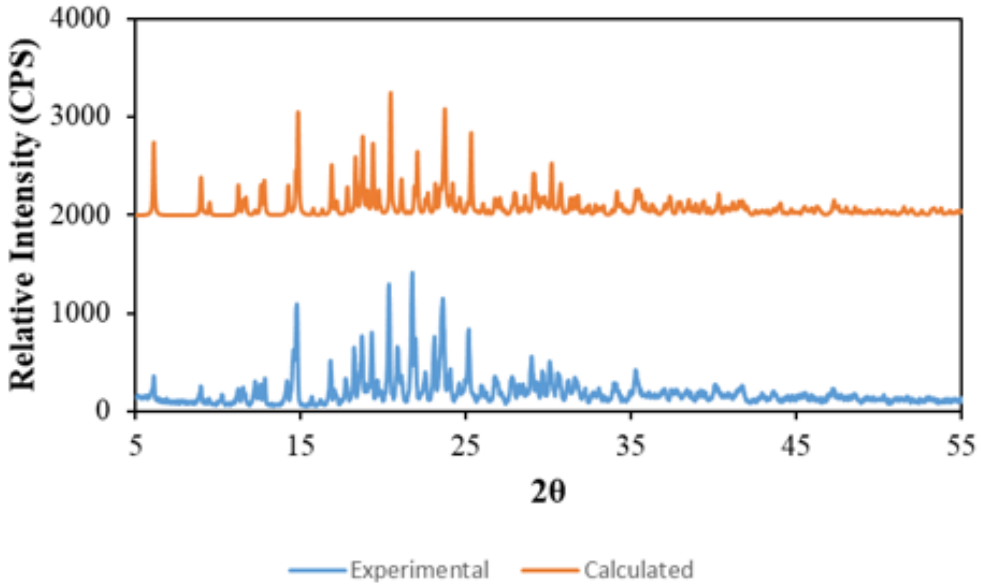

Figure A.4: Experimental and calculated powder X-ray diffractograms of **2b**, (3-iodoethynylbenzoic acid)$_2$ (propyltriphenylphosphonium bromide).

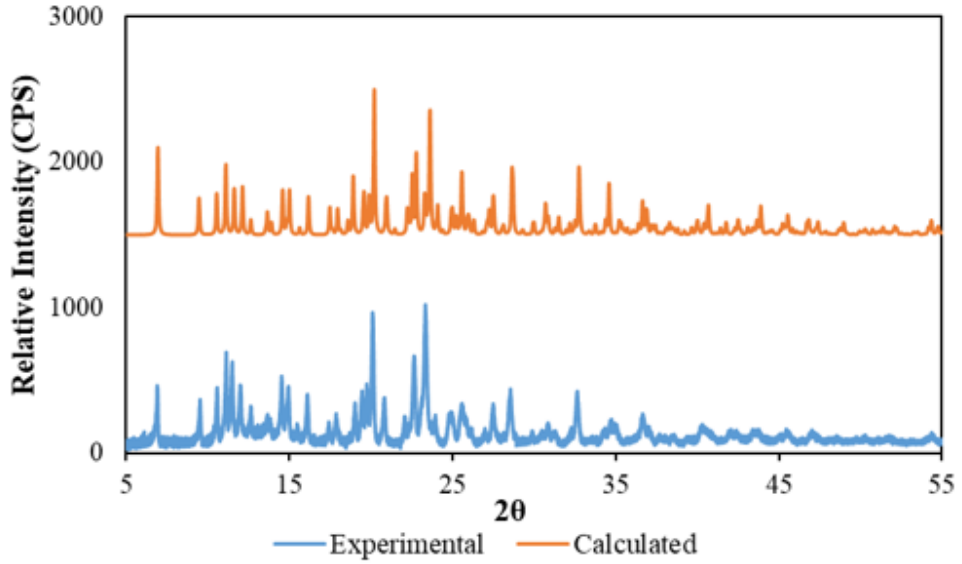

Figure A.5: Experimental and calculated powder X-ray diffractograms of **2c**, (3-iodoethynylbenzoic acid) (cyclohexyltriphenylphosphonium bromide).

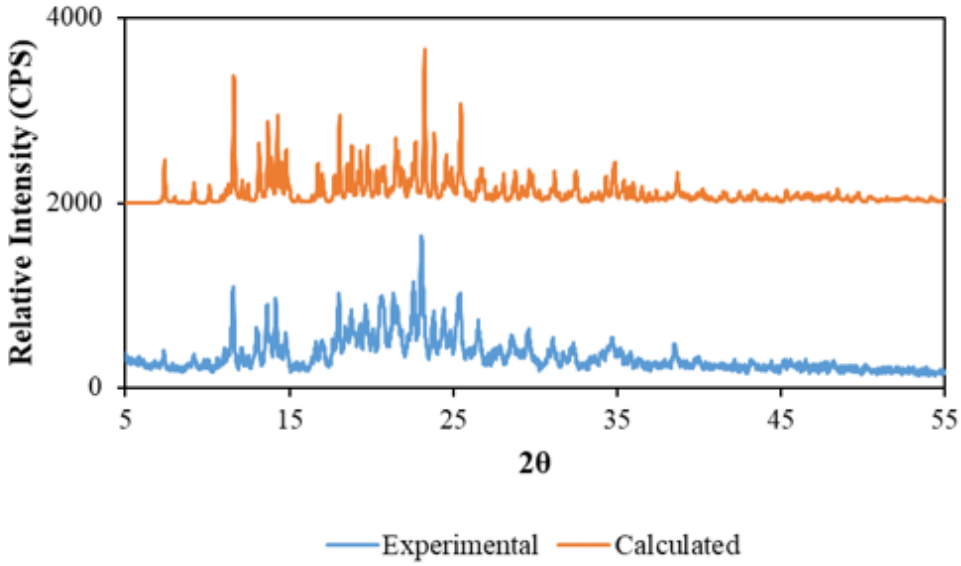

Figure A.6: Experimental and calculated powder X-ray diffractograms of **2e**, (3-iodoethynylbenzoic acid) (bis[triphenylphosphoranylidene]ammonium chloride)(ACN).

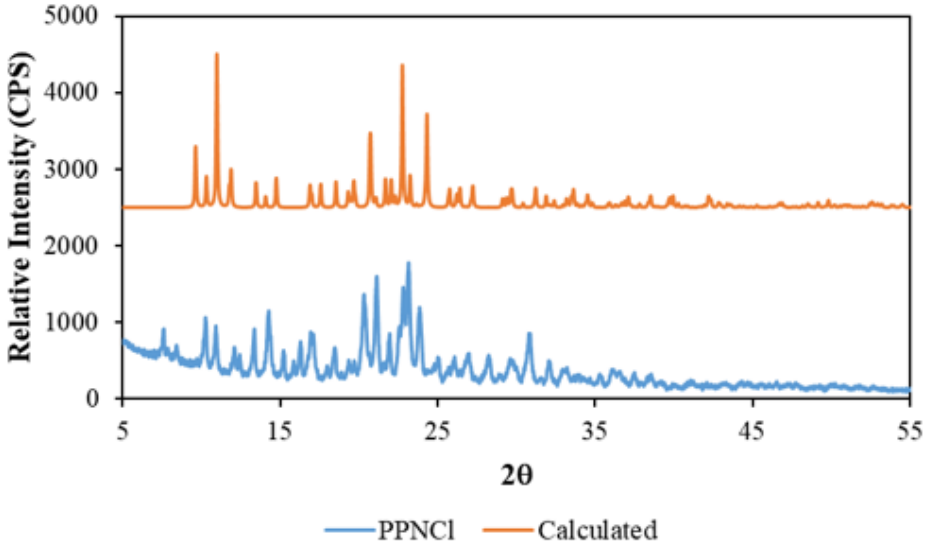

Figure A.7: Experimental and calculated powder X-ray diffractograms of compound **e** (PPNCl). The experimental trace, in blue, is from the as-received powder used for our reactions and for SSNMR experiments. The calculated trace, in orange, is generated from the reported single-crystal X-ray structure (Knapp and Uzun, *Acta Cryst.*, **2010**, *E66*, o3185). The traces do not match, indicating polymorphism.

A.3 ORTEP Plots

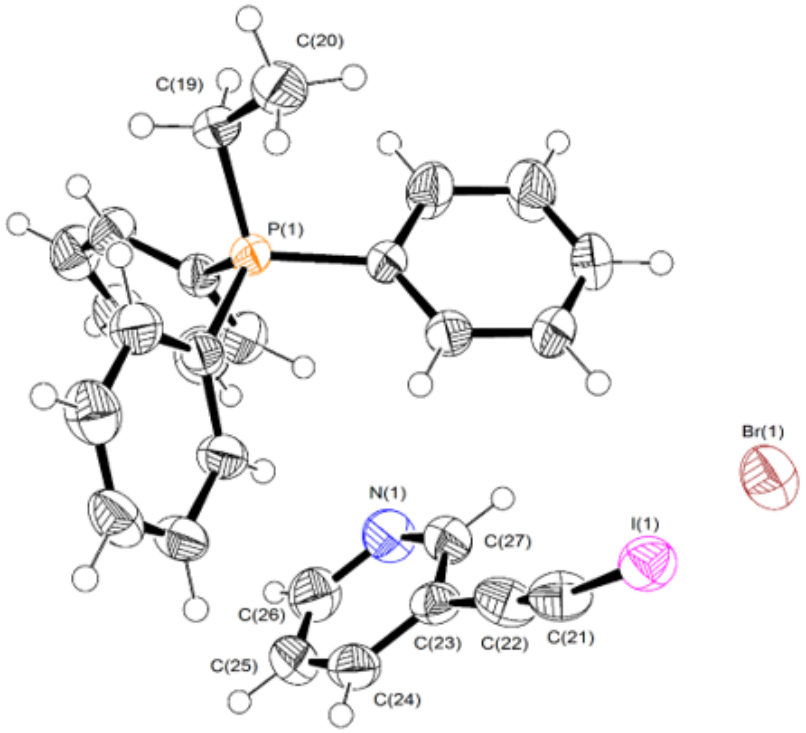

Figure A.8: Thermal ellipsoid plot of (3-iodoethynylpyridine) (ethyltriphenylphosphonium bromide) (**1a**).

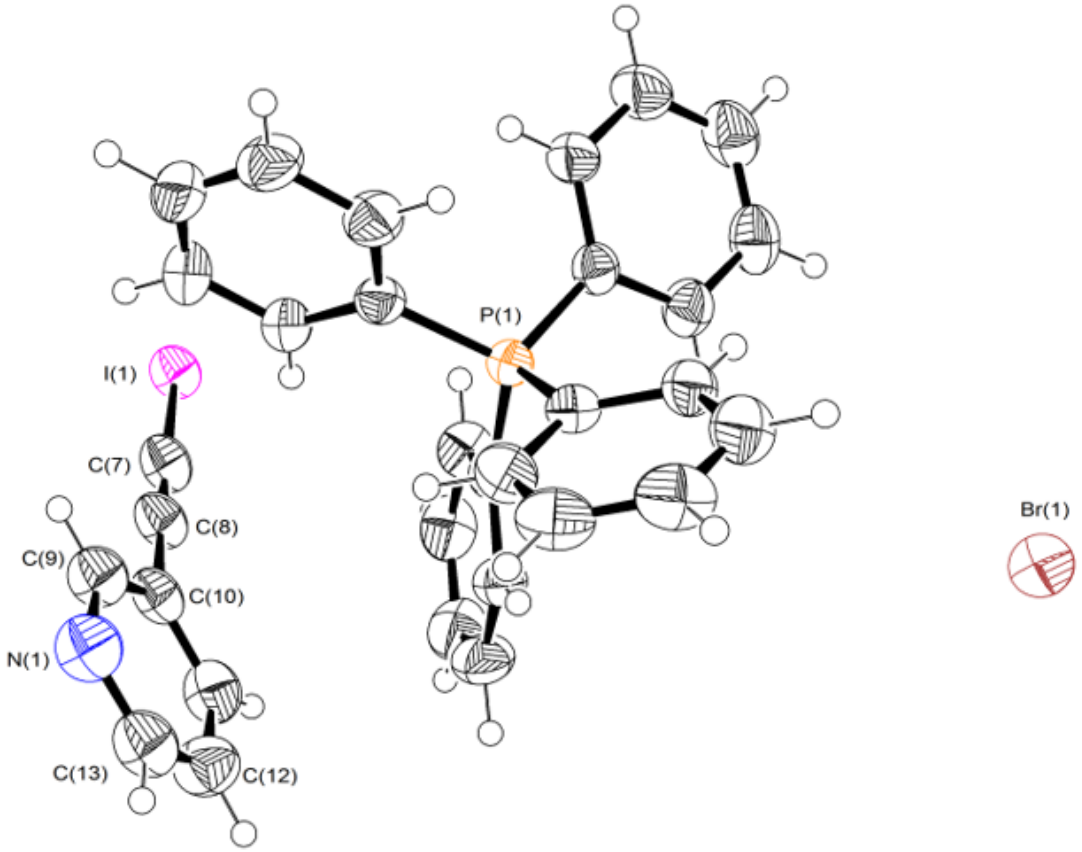

Figure A.9: Thermal ellipsoid plot of (3-iodoethynylpyridine) (tetraphenylphosphonium bromide) (**1d**).

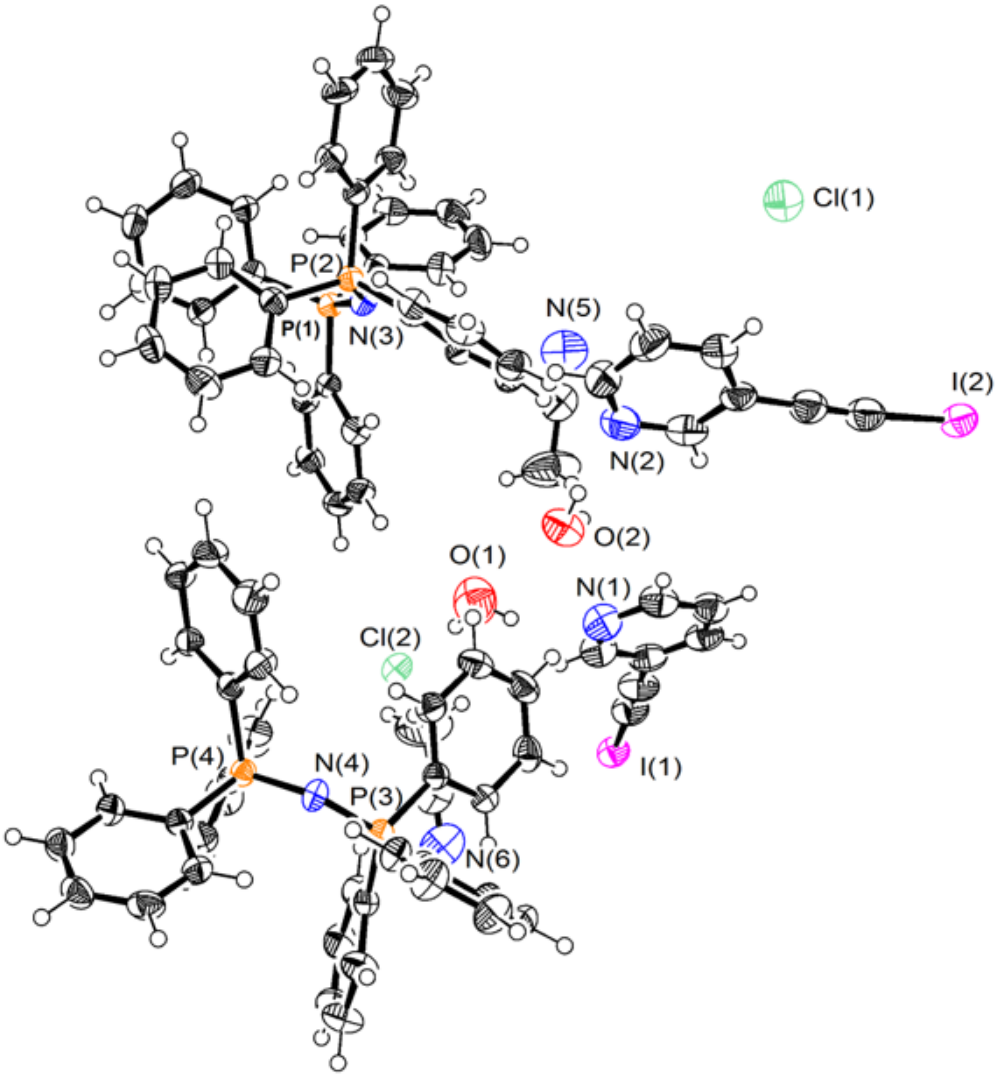

Figure A.10: Thermal ellipsoid plot of (3-iodoethynylpyridine)$_2$ (bis[triphenylphosphoranylidene] ammonium chloride)$_2$ $(H_2O)_2$ $(ACN)_2$ (**1e**).

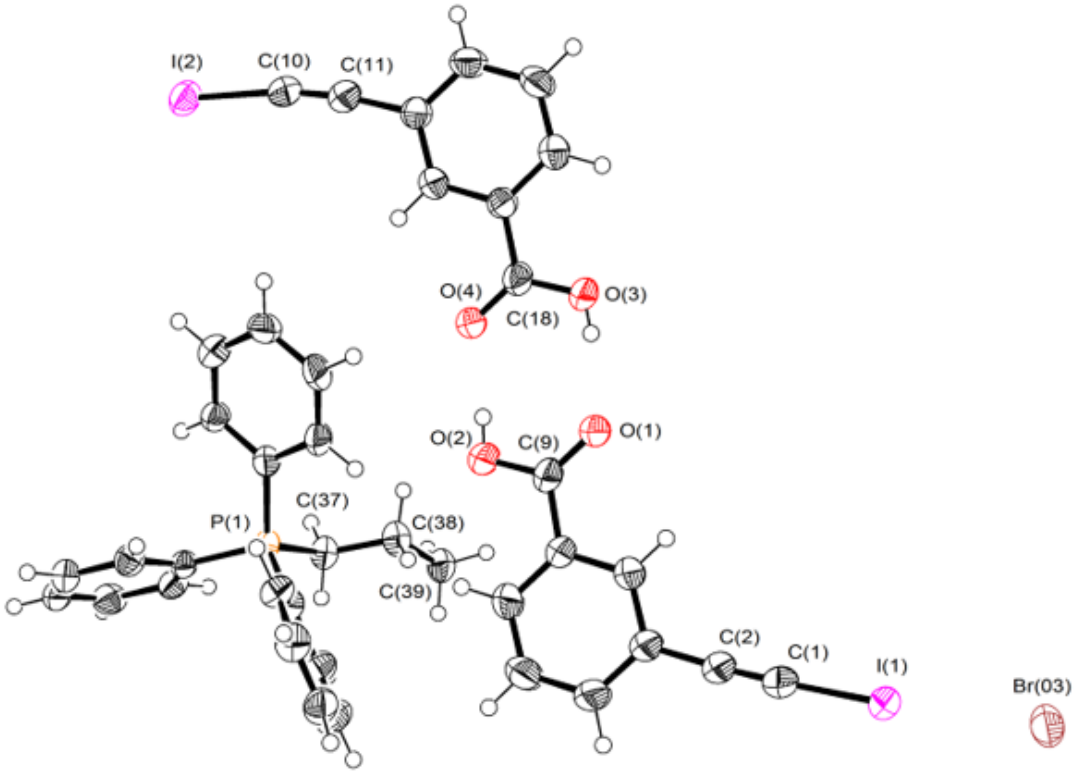

Figure A.11: Thermal ellipsoid plot of (3-iodoethynylbenzoic acid)$_2$ (propyltriphenylphosphonium bromide) (**2b**).

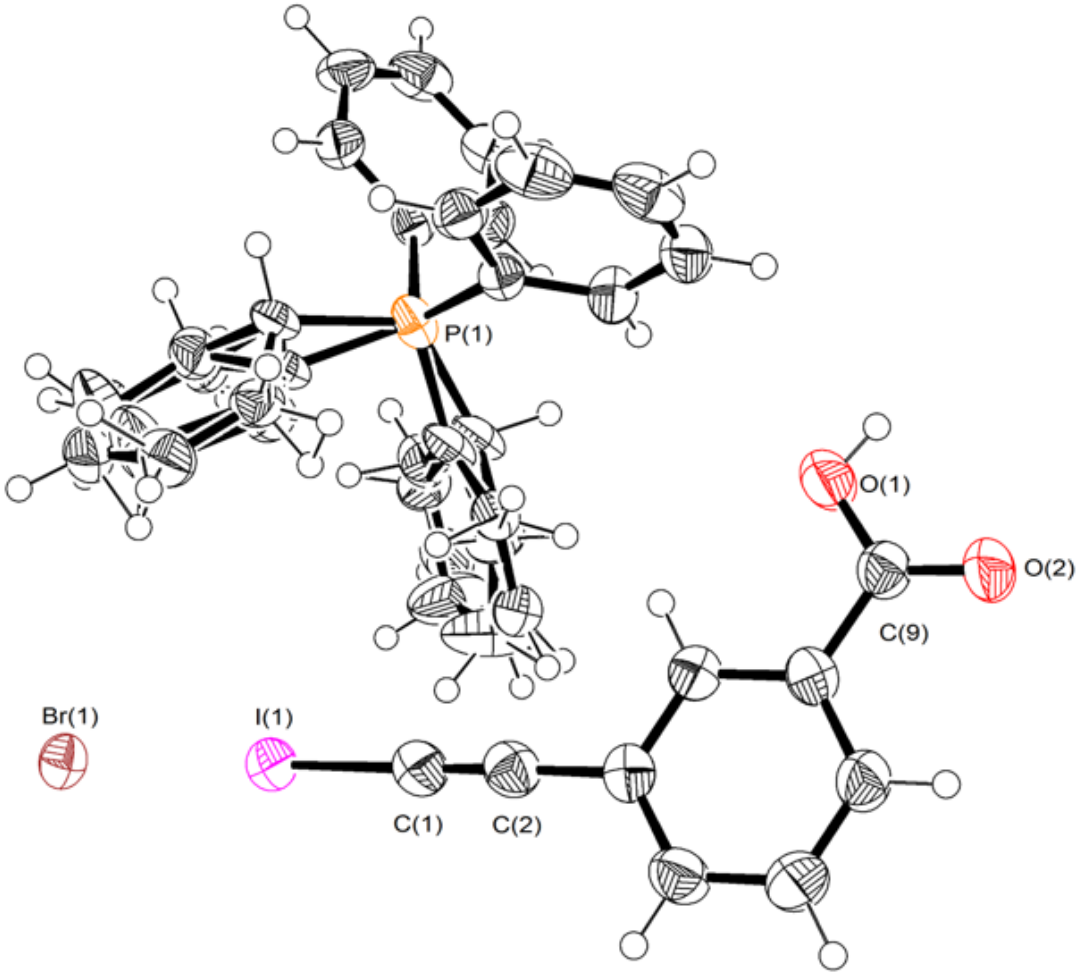

Figure A.12: Thermal ellipsoid plot of (3-iodoethynylbenzoic acid) (cyclohexyltriphenylphosphonium bromide) (**2c**).

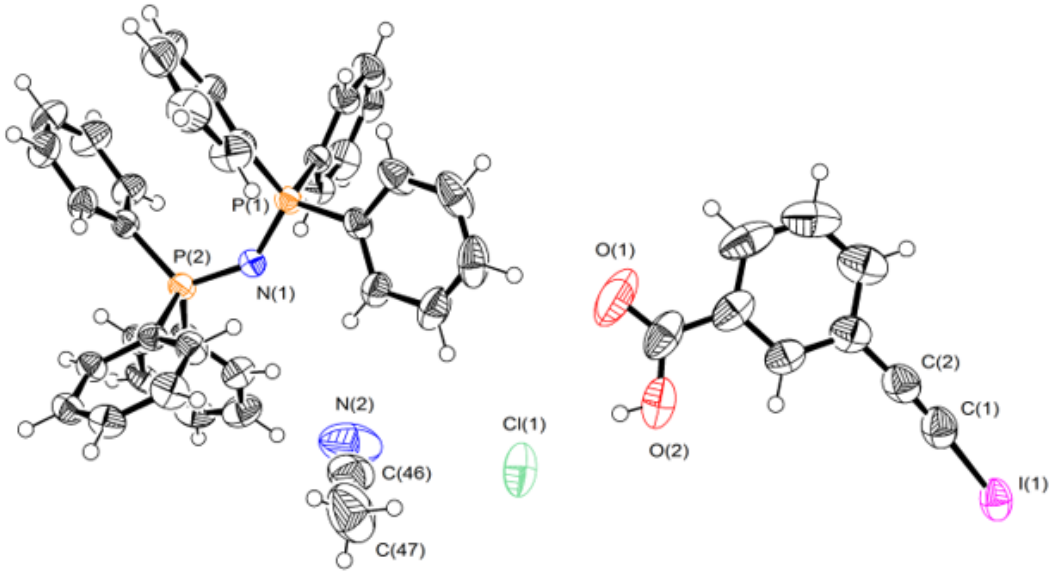

Figure A.13: Thermal ellipsoid plot of (3-iodoethynylbenzoic acid) ((bis[triphenylphosphoranylidene] ammonium chloride)(ACN) (**2e**).

A.4 NMR Spectra

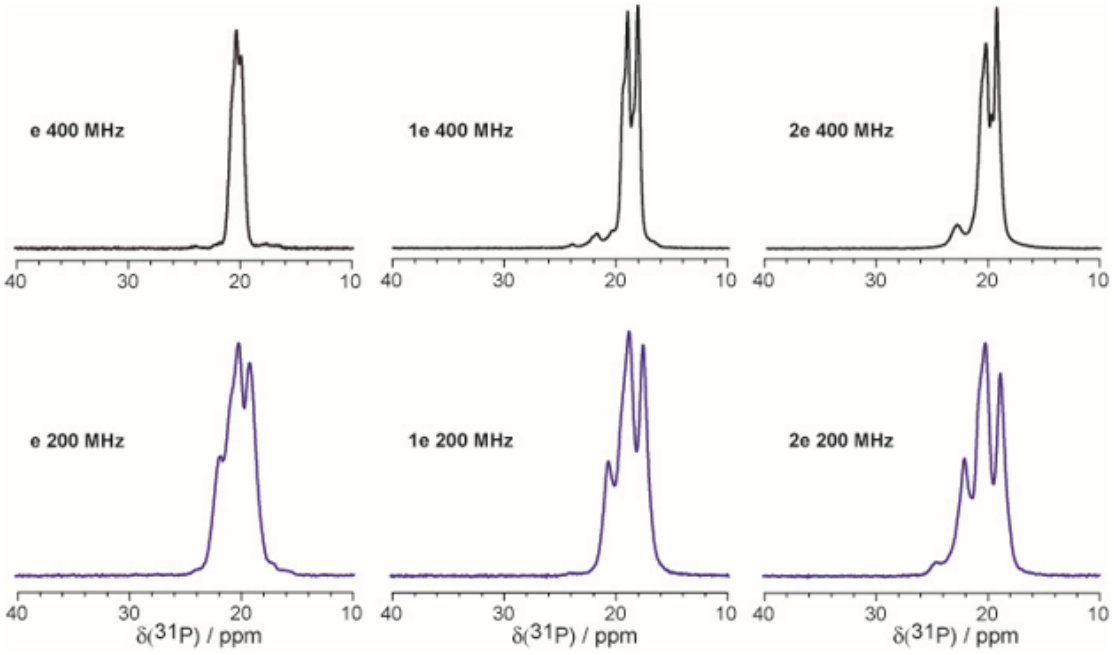

Figure A.14: ^{31}P CP/MAS NMR spectra of compounds **e**, **1e**, and **2e** acquired on 200 and 400 MHz spectrometers. Spectral narrowing in the higher applied magnetic field is consistent with the explanation that residual dipolar coupling to ^{14}N is in part responsible for the observed broadening and splitting of the resonances.